

AD-A240 200

DUCE AT GOVERNMENT EXPENSE



(1)

SE

## REPORT DOCUMENTATION PAGE

1a REPORT SECURITY CLASSIFICATION Unclassified			1b RESTRICTIVE MARKINGS			
2a SECURITY CLASSIFICATION AUTHORITY Unclassified			3 DISTRIBUTION/AVAILABILITY OF REPORT This document has been approved for public release and sale; its distribution is unlimited.			
2b DECLASSIFICATION/DOWNGRADING SCHEDULE						
4. PERFORMING ORGANIZATION REPORT NUMBER(S)			5. MONITORING ORGANIZATION REPORT NUMBER(S)			
6a. NAME OF PERFORMING ORGANIZATION Case Western Reserve University		6b. OFFICE SYMBOL (If applicable)	7a. NAME OF MONITORING ORGANIZATION Office of Naval Research; Dr. S. Fishman			
6c. ADDRESS (City, State, and ZIP Code) Department of Macromolecular Science Case Western Reserve University 10900 Euclid Ave. Cleveland, OH 44106-7202			7b. ADDRESS (City, State, and ZIP Code) 800 N. Quincy St. 704 Arlington, VA 22217			
8a. NAME OF FUNDING/SPONSORING ORGANIZATION Office of Naval Research		8b. OFFICE SYMBOL (If applicable)	9. PROCUREMENT INSTRUMENT IDENTIFICATION NUMBER N00014-89-J-1421			
8c. ADDRESS (City, State, and ZIP Code) 800 N. Quincy St. 704 Arlington, VA 22217			10. SOURCE OF FUNDING NUMBERS			
			PROGRAM ELEMENT NO	PROJECT NO	TASK NO	WORK UNIT ACCESSION NO
11. TITLE (Include Security Classification) Fracture Toughness of Carbon/Carbon Composites						
12. PERSONAL AUTHOR(S) A. Moet and J. Minick						
13a. TYPE OF REPORT Final		13b. TIME COVERED FROM 4/1/89 TO 6/30/91		14. DATE OF REPORT (Year, Month, Day) 1991 July 27		15. PAGE COUNT 135
16. SUPPLEMENTARY NOTATION						
17. COSATI CODES			18. SUBJECT TERMS (Continue on reverse if necessary and identify by block number)			
FIELD	GROUP	SUB-GROUP				
			Composites; carbon/carbon fracture toughness; phenolic; pitch; PAN; rayon; microdefect			
19. ABSTRACT (Continue on reverse if necessary and identify by block number) SEE NEXT PAGE						
20. DISTRIBUTION/AVAILABILITY OF ABSTRACT <input checked="" type="checkbox"/> UNCLASSIFIED/UNLIMITED <input checked="" type="checkbox"/> SAME AS RPT <input type="checkbox"/> DTIC USERS						
22a. NAME OF RESPONSIBLE INDIVIDUAL Prof. A. Moet			22b. TELEPHONE (Include Area Code) 216-368-6654		22c. OFFICE SYMBOL	
21. ABSTRACT SECURITY CLASSIFICATION						

## ABSTRACT

The fracture toughness parameter,  $K_{max}$ , was used to measure the resistance of 2D and 3D carbon/carbon composites to crack initiation.  $K_{max}$  as a function of geometry and thickness was measured for two 2D composites differing in their fiber and matrix precursors, weave pattern and microdefect field. One composite, KKarb C had an average  $K_{max}$  of  $5.4 \text{ MPa}\cdot\text{m}^{1/2}$  and was independent of geometry and thickness. The second, T300 HT had an average value of  $16 \text{ MPa}\cdot\text{m}^{1/2}$  for the four-point bend and compact-tension geometries and a value of  $26 \text{ MPa}\cdot\text{m}^{1/2}$  for the single-edge notch configuration. The latter result occurs due to the composite strength and the interaction of the stress and microflaw fields. Also, the SEN samples had larger active zones leading to greater crack initiation resistance.

The effects of notch orientation and depth were analyzed for the 3D material. The circumferential testing direction showed the highest  $K_{max}$  values for all three notch depths because the crack front encountered the highest cross-sectional area of yarns. In the radial and circumferential directions  $K_{max}$  decreased as a function of increasing notch depth. In the axial direction no dependence on notch depth was found. A fractographic analysis of an axially-notched sample showed that the lack of toughening mechanisms resulted in a lower  $K_{max}$  value ( $1.9 \text{ MPa}\cdot\text{m}^{1/2}$ ) at a notch depth of 0.2

compared to the radial ( $5.2 \text{ MPa}\cdot\text{m}^{1/2}$ ) and circumferential ( $7.8 \text{ MPa}\cdot\text{m}^{1/2}$ ) notching directions. Lastly, a PASCAL program was written to compute the crack diffusion model parameters  $\gamma^*$ ,  $\gamma_{\min}$ , and  $\alpha$ . A higher value of  $\gamma^*$  for the 2D materials reflected the type, distribution, and size of flaws for the 2D materials. The  $\alpha$  parameter was lower for materials showing a high degree of fluctuation in their maximum load. The program has been run for the 3D composite and preliminary results reflect the diffusivity of the strength field.

## Table of Contents

	page
Abstract	ii
1. Introduction to C/C Composites and Fracture	1
1.1 Fracture Mechanics	7
1.2 LEFM and Composite Materials	8
2. Two-Dimensional C/C Composites	13
2.1 Introduction	13
2.2 Experimental	14
2.2.1 Material Description	14
2.2.2 Test Procedure and Data Analysis	17
2.3 Results and Discussion	23
2.3.1 Flaw Characterization	24
2.3.2 Load-Displacement Curves	28
2.3.3 Fracture Toughness	34
2.3.3.1 LEFM Considerations	34
2.3.3.2 $K_{max}$	37
2.3.4 Mechanistic Analysis	42
2.3.4.1 $KKarb$ C Composite	43
2.3.4.2 T300 HT Composite	49
2.4 Conclusions	59
3. Three-Dimensional C/C Composites	61
3.1 Introduction	61
3.2 Experimental	62
3.2.1 Material and Test Description	62
3.3 Results and Discussion	67
3.3.1 Microstructure	67
3.3.2 Fracture Toughness as a Function of Notch Orientation	73
3.3.2.1 $K_{max}$ Values	74
3.3.2.2 Load-Displacement Curves & Mechanistic Analysis	76
3.3.3 Fracture Toughness as a Function of Notch Depth	95
3.4 Conclusions	98
4. Crack Diffusion Model	100
4.1 Introduction	100
4.2 Model Derivation	101
4.3 Data Analysis	104
4.4 Results and Discussion	106
4.4.1 2D Composites	106
4.4.2 3D Composite	116
4.5 Conclusions	122
5. Conclusions	123
References	126
PASCAL program for 3D composite	131

## INTRODUCTION TO C/C COMPOSITES AND FRACTURE BEHAVIOR

Composites have become a class of materials whose implementations increase rapidly as the number of compatible matrices and fibers in existence grows. Available matrices range from ductile aluminum to brittle silicon nitride and epoxy resins. Fibers, either discontinuous or continuous generally have diameters greater than  $7\mu\text{m}$  which distinguishes them dimensionally from whiskers. The production of both precursors and the final composite involves a variety of techniques [1].

Since the "accidental" discovery of the reasonable strength of a phenolic resin char residue in 1958, the development of carbon/carbon (C/C) composites has spread into the aerospace, automobile, and biomedical industries [2]. C/C composites are derived from a range of fibers and matrices which differ in their degree of graphitizability and end mechanical properties depending upon their initial carbonaceous form [3]. Carbon fibers can be made from polyacrylonitrile (PAN), rayon, and mesophase (MP) pitch [4]. Due to their low tensile strength, the use of rayon fibers has been phased out and the drive to obtain high moduli PAN and MP pitch fibers at lower cost has intensified. The production of PAN fibers involves stretching and then heating to temperatures at which the  $\text{NH}_2$  groups react and form a ladder structure. The fibers are treated to promote oxidation and further cross-linking between the pendant groups [5]. The

turbostratic graphitic structure is obtained during additional stretching at graphitization temperatures above 2500°C. Mesophase pitch fibers were first produced economically by Singer at Union Carbide in the late 1970s [6]. In this process fibers from an acenaphthylene pitch were melt spun and drawn through a die at 400°C where the mesophase globules coalesced and were oriented along the axial direction.

The moduli of PAN fibers may reach 650 GPa [7] if graphitized under stress. Most industrial processes produce fibers with moduli between 300 and 400 GPa since the process to produce high modulus fibers is not economical [8]. Pitch fibers may be manufactured with moduli of 800 GPa [9] which approaches the theoretical modulus of graphite (1000 GPa). The high modulus results in two undesirable features: 1) low ultimate tensile strength (1-3 GPa) [4] and, 2) a low strain to failure. The strength is also limited by the distribution of voids and surface flaws along the length of the fiber which act as stress concentrators. Also, since the higher modulus fibers possess a more graphitic structure, the interfacial adhesion to the matrix decreases because of the perfect crystalline state and lack of available mechanical cohesive sites [2].

Common matrices for C/C composites are resins and coal pitches. Ideally the precursor should have a high char yield, good flow properties at the processing temperatures, and

sufficient compatibility with the fiber to promote desirable interfacial properties. Phenolic resins are cross-linked materials which resist orientation and therefore remain brittle and more isotropic than matrices which show preferential orientation. Pitch is desirable due to its high char yield and strength, lower shrinkage and ability to be processed over a wide temperature range [10]. Two methods are commonly used to manufacture C/C composites: chemical-vapor deposition (CVD) and impregnation. In the former the fibers are coated with matrix using a hydrocarbon gas to infiltrate the fiber preform. The latter method involves multiple infiltrations of the matrix around the preform. The microstructure is determined by the ability of the matrix to penetrate between the yarns. Impregnation is often used with CVD in order to obtain a high density composite [11].

Although the early research focused on unidirectional composites [12-14], research in the 1970s was directed towards two and three-dimensional composites [15-17]. The development of 2D composites began with cross-ply laminates consisting of multiple unidirectionally aligned fibers with alternating angles between plies. A second type of 2D composite is constructed from woven plies which are then stacked and cured to form a laminated material. The weave types range from a plain weave in which the number of yarns in each direction is equal to harness weaves which are unbalanced. The major

drawback to 2D composites is that they fail in shear along the plies due to the low interlaminar shear strength. Multi-directional materials with reinforcement perpendicular to the plies were developed for applications such as rocket nozzles [18]. In this process yarns are placed on a mandrel in the radial direction through which circumferential and axial yarns are woven. The radial yarns prevent interfacial shear by confining the movement of the circumferential and axial yarns. Other 3D configurations consist of 1) cubic arrays or 2) constructions in which the direction of highest yarn density is based upon the application.

Given the variety of processing conditions and precursors available for C/C composites the prediction of general behavior is not feasible. The microstructural interactions, i.e., at the yarn-matrix, fiber-fiber, and fiber-matrix levels must be considered. In this respect then, the researcher is confined to explaining micro and macromechanical behavior for a particular system.

A number of studies on the mechanical properties of 2D [19-21] and 3D [17, 22-25] composites have been carried out. The effects of CVD conditions, specifically temperature, substrate characteristics, and carrier gas concentration on the 2D composite dominant failure mode and fiber/matrix bonding was investigated [19]. It was found that catastrophic failure occurred when strong fiber-matrix interlocking



promoted fiber failure rather than pullout and delamination. Further work performed by Kowbel and Shan [20] sought to elucidate the type of chemical species present along the fibers. They employed surface-treatment techniques to introduce specific functional groups on the fiber surface and then correlated the flexural strength with the resulting proposed interfacial structure.

The macrostructure of a 2D composite also influences the mechanical behavior [21]. In this work, 2D composites woven into 8-harness and plain weave configurations were characterized to determine how the weave periodicity influenced the ability of the matrix to penetrate the weave. It was found that the development of thermal stress microcracks in the more tightly woven plain weave material resulted in catastrophic failure. In contrast, the looser yarns of the harness weave were able to accommodate thermal expansion differences and showed pseudo-plastic failure accompanied by fiber pullout.

Similar characterization of 3D materials has employed finite element analysis modelling due to the complexity of the microstructure. Such studies include the viscoelastic response of the matrix during processing [22] and transient thermal conduction [23]. Assessment of the microstructure created during processing was pioneered by Sines and Cohen [24]. The purpose was to correlate the development of

fabrication stresses and microstructure. Subsequent work by Jortner [25] led to the conclusion that microcracks created as a result of thermal expansion mismatch between mutually perpendicular fibers and matrix shrinkage weakened the interface. Consequently the tensile strength was reduced but a higher toughness was achieved due to the facilitation of fiber pullout.

Two studies [26,27] monitored the microstructure development during the impregnation, carbonization and graphitization cycles. After specific processing steps specimens were tested in flexure and tension. It was found that gaps formed after graphitization around radial yarns leading to a decrease in both flexural and tensile strengths in this direction. Strength was maintained in the other two directions since the yarns were able to freely expand and contract during thermal cycling.

A paper on interfaces in 3D composites [28] called for a more thorough understanding of the creation of interfacial microstructure and the influence of processing on the same. It is also evident from the literature review that the use of fracture mechanics derived for metals is not always adequate in describing the complex failure behavior. Before discussing the results of this work some basic concepts of fracture mechanics and their applicability to composite materials will be reviewed.

### 1.1 Fracture Mechanics

The behavior of a material containing a flaw under stress was first characterized by Griffith [29]. He proposed that the kinetics for crack growth are favored when the surface energy increase supersedes the release of elastic strain energy. At equilibrium the two processes will be equal:

$$(1) \quad \frac{dU}{da} = 0 = \frac{d}{da} \left[ 4a\gamma - \frac{\pi a^2 \sigma^2}{E} \right]$$

where  $a$  is the crack length,  $\gamma$  the surface energy,  $\sigma$  the applied stress,  $E$  Young's modulus, and  $U$  the potential energy. The stress is then related to the crack length and surface energy by:

$$(2) \quad \sigma = \sqrt{\frac{2\gamma E}{\pi a}}$$

Crack growth occurs at a critical flaw size and stress denoted  $a_c$  and  $\sigma_c$  respectively:

$$(3) \quad \sigma_c = \sqrt{\frac{2\gamma E}{\pi a_c}}$$

For brittle materials the criterion is valid but the surface energy term accounts only for elastic deformation. Irwin [30] extended the surface energy term to include plastic work,  $\gamma_p$ :

$$(4) \quad \sigma_c = \sqrt{\frac{2(\gamma + \gamma_p) E}{\pi a_c}}$$

The work required to create new surfaces was called the crack extension force,  $G$ , and equation 4 is rewritten as:

$$(5) \quad G = \sigma^2 \frac{\pi a_c}{E}$$

The processes occurring at the crack tip were described by Irwin [31]. The stress intensity factor,  $K$ , related the bulk applied stress,  $\sigma$ , to the flaw size,  $a$ , and the load-specimen geometry through the  $f(a/W)$  term:

$$(6) \quad K = \sigma \sqrt{\pi a} f(a/W)$$

By comparison with equation five:

$$(7) \quad K^2 = GE$$

In plane strain where the plastic zone is small relative to the specimen thickness:

$$(8) \quad K^2 = \frac{GE}{(1 - \nu^2)}$$

Equation 7 then represents the less severe loading conditions of plane-stress.

## 1.2 Linear Elastic Fracture Mechanics and Composite Materials

The stress-intensity factor is a material parameter which serves as a measure of crack resistance for brittle materials. As such certain guidelines have been established which permit the use of  $K^{IC}$  as a design criterion. Firstly, specimen dimensions established in ASTM E399 [32] for Mode I loading are chosen to maintain plane-strain at the crack tip:

$$a, B \geq 2.5 \left( \frac{K_{IC}}{\sigma_y} \right)^2$$

where  $\sigma_y$  is the yield stress and B the specimen thickness. Ideally brittle materials show a plane-stress/plane-strain transition with thickness (Figure 1.1) and the engineer designs for plane-strain conditions.

Secondly,  $K_{IC}$  is a valid fracture toughness when the crack remains planar as in the case of metals. However, the development of a plastic zone as a result of crack tip blunting results in non-collinear crack growth. In the case of composite materials the non-collinear crack growth reflects the ability of the fibers to deflect and direct cracks out of the notch plane.

The test conditions should also insure that the occurrence of crack propagation prior to ultimate failure is minimized. "Pop-ins" indicate that processes other than crack growth at the notch tip are present.

The a priori application of LEFM to C/C composites has been examined for unidirectional materials [33-35]. Most modelling has considered the composite as a homogeneous continuum or as a series of segments in which the micromechanical behavior is related only to crack tip processes [36]. The significant failure mechanisms include fiber debonding and pullout, crack bridging by intact fibers

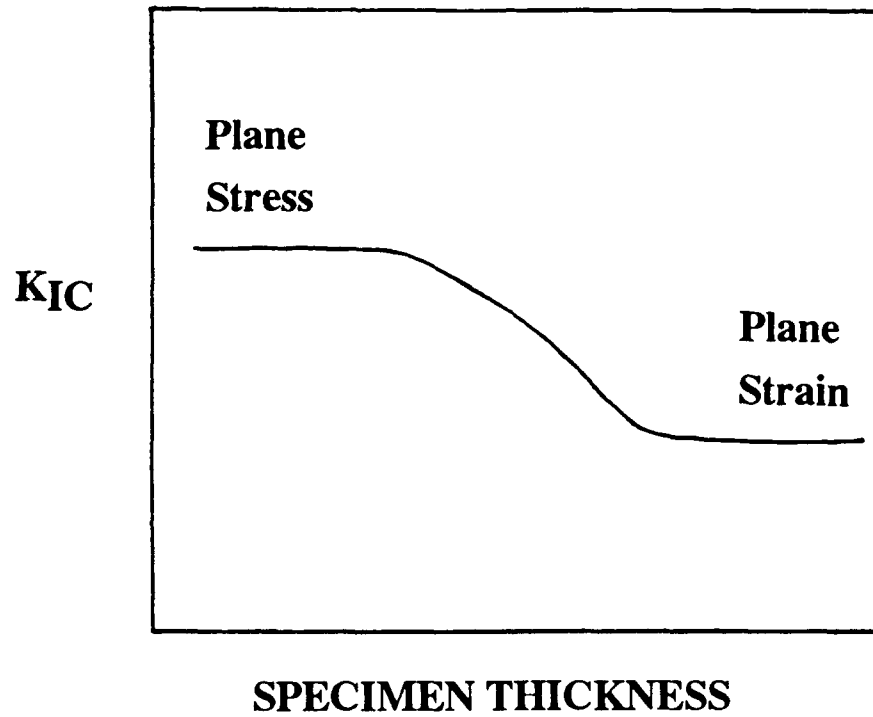


Figure 1.1  $K_{IC}$  as a function of specimen testing thickness,  $t$ , showing the plane-stress to plane-strain transition for ideal solids.

and matrix yielding. In general the predicative models do not incorporate the heterogeneity of the material reflected in the variety of fracture mechanisms.

The fracture toughness of 2D C/C composites has been measured using  $G_c$ ,  $K_c$  and the work-of-fracture (WOF) [37] as well as the R-curve and J-integral techniques [38]. The latter study focused on the effects of weave type. It was concluded that the mode of crack propagation was dependent on the notch orientation and that the resistance to fracture decreased as a function of notch depth. The work by Guess and Hoover [37] showed that both  $K_c$  and  $G_c$  were independent of notch depth and as such could be designated material parameters for the particular testing conditions. However, the work of fracture was a decreasing function of notch depth. Although the WOF did not measure the surface energy created it served as a ranking parameter for different materials under identical testing conditions.

The amount of work done to measure the fracture toughness of 3D composites has been limited [39-40]. In the current work the resistance to crack initiation for both 2D and 3D composites has been measured using  $K_{max}$ . The 2D composites differed in their precursors, weave type, and microdefect field. Both were tested to determine the dependence of  $K_{max}$  on specimen geometry and thickness. The dependence of  $K_{max}$  on notch depth and orientation was measured for a 3D cylindrical

billet with different yarn densities in two of the three directions. Lastly, the crack diffusion model which incorporates the statistical nature of crack propagation with fracture mechanics is introduced. Two parameters are abstracted which are related to the microstructure and strength field. The results obtained from a PASCAL program written for a PC are compared to those from the VAX system previously used.



**CHAPTER 2**

**FRACTURE TOUGHNESS OF 2D COMPOSITES**

## 2.1 INTRODUCTION

The emergence of C/C composites as viable structural materials dictates that an understanding of the fracture behavior be developed to insure proper part design and rational material development. A number of studies [20,37,38,41] employing linear elastic fracture mechanics (LEFM) to evaluate the fracture toughness of 2D C/C composites have been carried out. Most of these studies have focused on the effects of notch depth and orientation [37,38] and precursor properties [20,41] on the fracture toughness. Variations in  $K_{max}$  with specimen thickness and geometry have not been thoroughly explored.

The plane stress-plane strain transition of  $K_{Ic}$  with specimen thickness witnessed in monolithic materials is not expected in C/C composites since the plastic zone which increases the fracture resistance has not been observed in C/C composites. The source of toughening over the pure brittle carbon components may be attributable not only to the processing-induced microdefect field but the weave design [21]. The fracture toughness of linear elastic monolithic materials is also independent of test configuration. Geometric correction factors account for the imposed stress state at the crack tip for each load-specimen configuration [44]. However, no mathematical compensation exists for the interaction between crack tip stress state and the

hierarchical structure of the composite.

In this chapter, the dependence of the interlaminar fracture toughness of two 2D C/C composites on specimen geometry and thickness will be examined. The two composites were fabricated from different fiber and matrix precursors. Additionally, each composite has been woven into a different warp-to-fill ratio. The microstructural flaw distribution and type will be related to the behavior manifested in the load-displacement curves. Lastly,  $K_{max}$  is calculated and correlated to the microstructural failure mechanisms at initiation.

## 2.2 EXPERIMENTAL

### 2.2.1 Material Description

A brief summary of the mechanical properties and densities of the two 2D C/C composites used in this investigation is listed in Table 2.1 [42,43]. The first, designated KKarb, type C, was obtained from Kaiser Aerotech Corporation in San Leandro, California. This composite is made from a phenolic resin matrix reinforced with a plain-woven (1:1) (Figure 2.1) fabric of yarns made from a rayon yarns. The weave is unbalanced with 22 fill yarns and 26 warp yarns per square inch. However, the warp and fill yarns contain the same number of fibers [42].

The second material, T300 HT was obtained from Acurex Corporation in Mountain View, California. The reinforcing

Table 2.1  
Physical Properties of 2D C/C Composites

Material	Fiber/Matrix	Density (g/cm <sup>3</sup> )	E (Warp) (GPa)	UTS (Warp) (MPa)
KKarb C	Rayon/Phenolic	1.51	15	61
T300 HT	PAN/Pitch	1.88	160	360

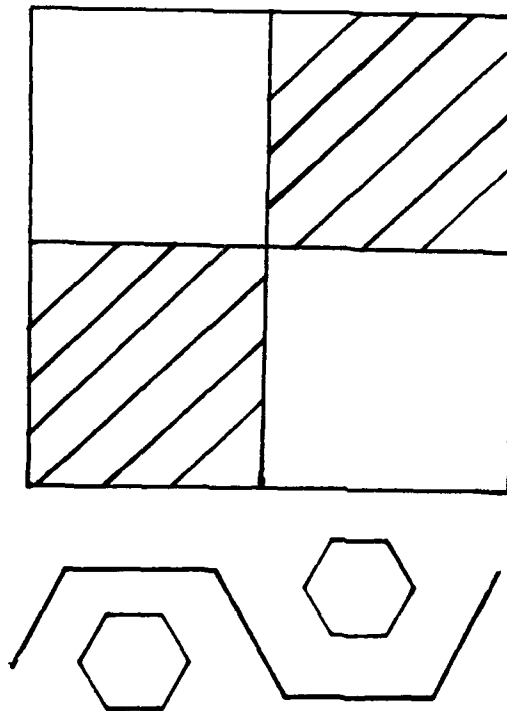


Figure 2.1 Plain-weave configuration for 2D KKarb C composite.

fibers are derived from a PAN precursor and woven into an 8-harness weave in a pitch matrix (Figure 2.2) [43]. Both materials were made into preforms and then repeatedly impregnated with matrix precursor and thermally processed to achieve the final density.

### 2.2.2 Test Procedure and Data Analysis

The chosen test configurations were compact-tension (CT), single-edge notch (SEN), and four-point bending (4PB) illustrated in Figures 2.3-2.5. The sample thicknesses and corresponding geometries are listed in Table 2.2. The maximum thickness was limited by the plate dimensions. In the case of both the 4PB and CT specimens a thickness of 1.5 mm could not be used since instabilities occurred during loading. Likewise, the SEN configuration was not tested at a thickness of 6.5 mm because of slippage in the grips. A notch was introduced into the 4PB and CT specimens using a 0.25 mm diamond-edged saw and then sharpened with a razor blade to the depths indicated. The notch was inserted into the SEN samples using a 60° notching blade. The specimens were loaded in an MTS machine at a crosshead speed of 0.25 mm/min under stroke control. Crack-opening as well as load-point displacement were measured as a function of load for each geometry.

The crack-opening displacement (COD) for SEN samples was measured by using an extensometer with a gage distance of 25.4

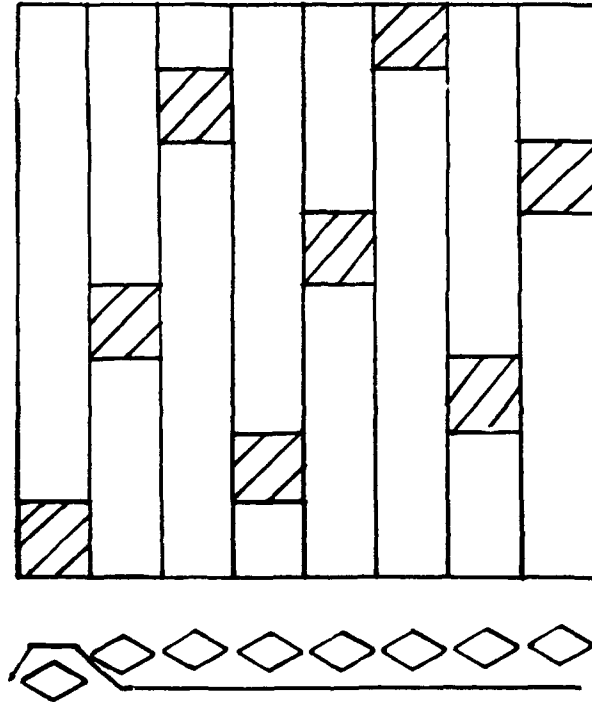
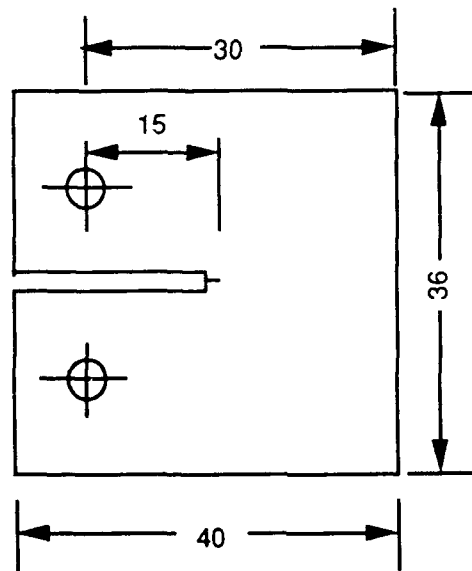


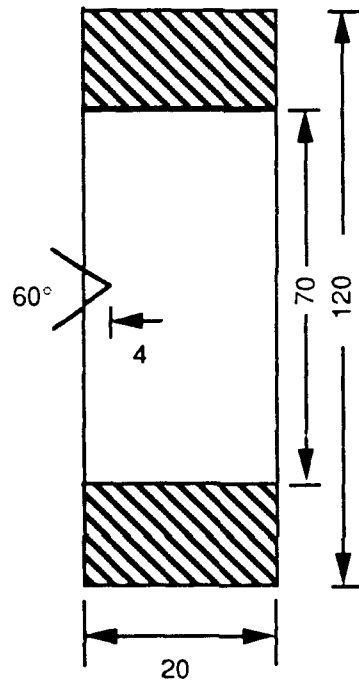
Figure 2.2 Harness-weave configuration for 2D T300 HT composite in which there are seven warp yarns per fill yarn.



All Dimensions in Millimeters

Figure 2.3. Compact-tension configuration for 2D testing.





All Dimensions in Millimeters

Figure 2.4. Single-edge notch configuration for 2D testing.

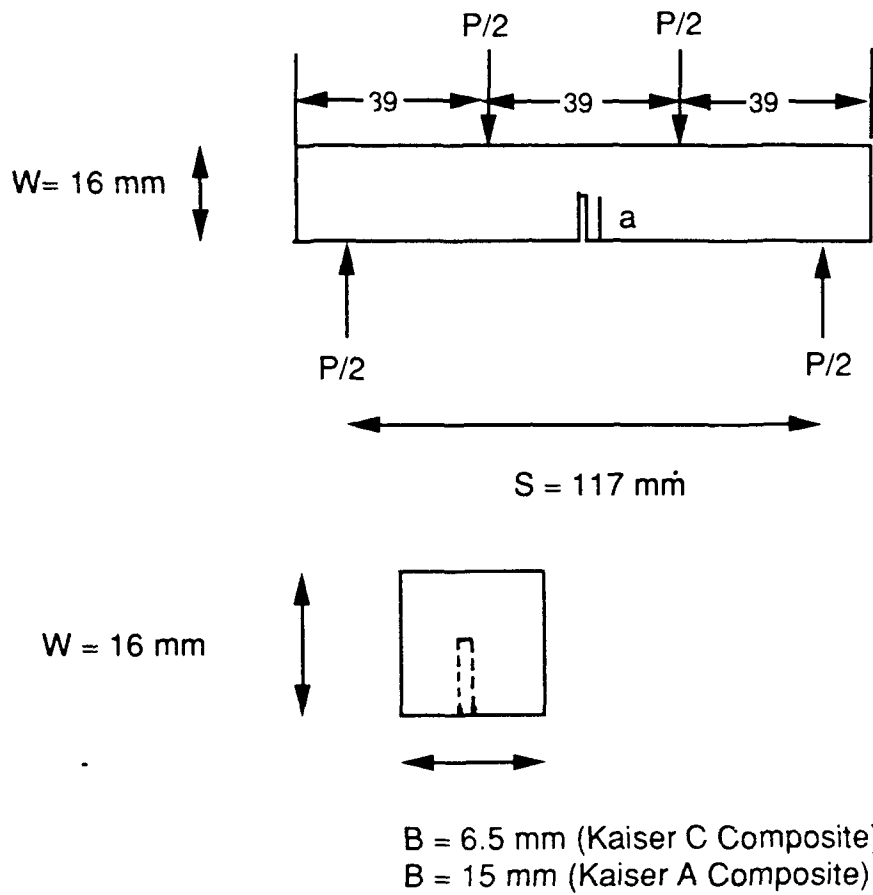


Figure 2.5. Four-point bend configuration for 2D testing.

Table 2.2  
Specimen Thickness and Respective Configuration

Thickness (mm)		Configuration	
6.5	4PB	CT	--
3.0	--	CT	SEN
1.5	--	--	SEN

mm placed on the surface. A clip gauge mounted on the notched side using knife edges was used to measure the COD of the 4PB and CT samples. The load and displacement signals were transferred as voltage output to a computer where they were digitized and then plotted on an x-y recorder. The fracture surfaces were examined using a JEOL JXA840 scanning-electron microscope. A micrograph used to characterize the flaw distribution in the KKarb C composite was obtained by flexing a 10 mm x 6 mm specimen with two screws at either end. Flexure of the specimen opened up the microcracks and facilitated computation of the microcrack population. The specimen and screws were mounted on an SEM stage and gold sputter-coated.

The geometric correction factors for 4PB, SEN, and CT configurations respectively, were [44]:

$$f(a/W) = 1.122 - 1.4(a/W) + 7.33(a/W)^2 - 13.08(a/W)^3 + 14(a/W)^4$$

$$f(a/W) = 1.12 - 0.23(a/W) + 10.55(a/W)^2 - 21.71(a/W)^3 + 30.382(a/W)^4$$

$$f(a/W) = \frac{(2+a/W) [0.886 + 4.6(a/W) - 13.32(a/W)^2 + 14.72(a/W)^3 - 5.6(a/W)^4]}{(1-a/W)^{3/2}}$$

### 2.3 RESULTS AND DISCUSSION

Since the two materials investigated differed in their strength, macrostructural design and microdefect type and

distribution, the analyses presented allow no generalizations about 2D C/C composites to be extracted. First, the nature and number of flaws in each composite are examined. Then, the load-displacement curves are discussed in order to explain the interdependence of flaw distribution and load configuration on the fracture behavior.  $K_{max}$  calculated from the maximum load is presented as a function of testing thickness and geometry. Lastly, a fractographic analysis used to elucidate the relationship between the hierarchical design, load-displacement behavior and  $K_{max}$  is discussed.

### 2.3.1 Flaw Characterization

Figure 2.6 shows a typical SEM micrograph of the unfractured KKarb C composite. Microcracks extend between the laminates normal to the weave direction. The microcracks are attributed to the processing during which tensile stresses develop in the matrix as a result of the thermal expansion coefficient differential between the matrix and yarns. In contrast to this appearance, the T300 HT specimen contains both microcracks and voids (Figures 2.7, 2.8). Voids lay between the warp and fill yarns and along the ply-matrix interfaces. The voids are present because of the viscous nature of the pitch matrix and its inability, therefore, to completely penetrate between the laminates. Voids and microcracks were distinguished based upon their location.

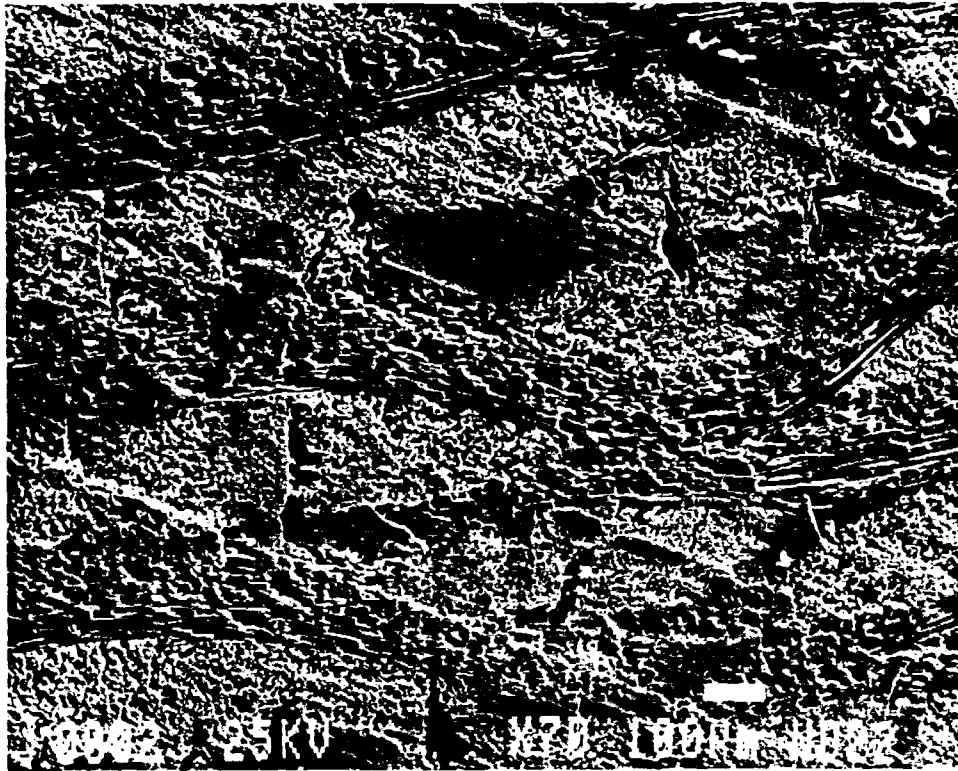


Figure 2.6. SEM micrograph of unfractured KKarb C composite showing microcracks between the plies.

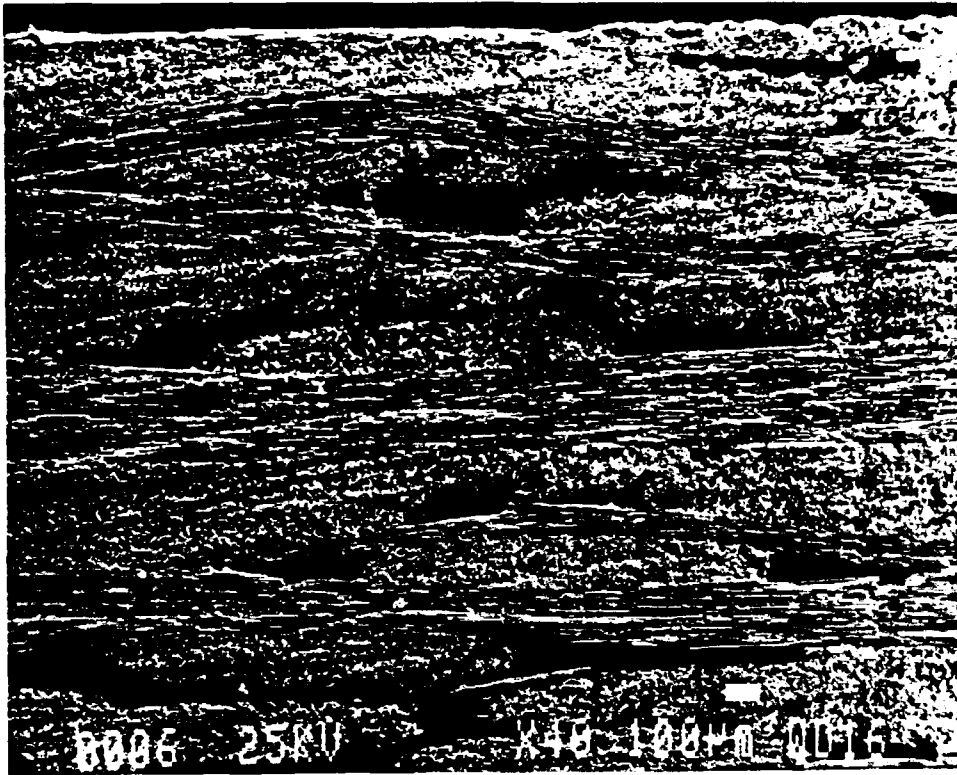


Figure 2.7. SEM micrograph of unfractured T300 HT composite showing voids along the plies.

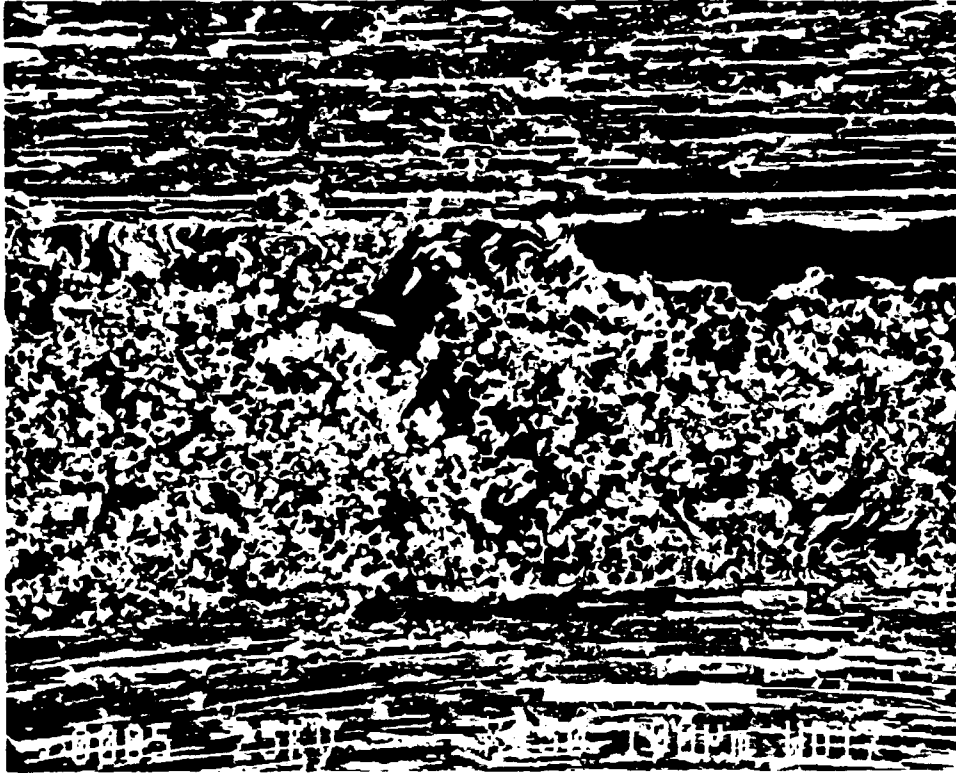


Figure 2.8. SEM micrograph of unfactured T300 HT composite showing microcrack through yarn bundle adjacent to a void.



Microcracks were generally assigned to be features running between the plies and voids along the plies.

Statistical distributions of the microcracks for KKarb C and T300 HT were calculated from micrographs similar to those in Figures 2.6 and 2.8. In both cases the average microcrack length is approximately 150  $\mu\text{m}$ . This distance corresponds approximately to the interweave spacing. The average number of microcracks per  $\text{cm}^2$  for the KKarb C composite is almost six times (2165) higher than that for the T300 HT material (375). The statistical distribution of microvoids in the T300 HT specimen was determined from a micrograph similar to Figure 2.7. The aspect ratio,  $L/h$ , is defined as the microvoid length to width. A circular void has a value of one and as the degree of eccentricity increases so does the aspect ratio. In this sample the highest population of voids has an  $L/h$  value of two at which the number average of voids per  $\text{cm}^2$  is 34. The second largest population is found at an aspect ratio of six with a density of 22 per  $\text{cm}^2$ . Therefore the distribution consists of primarily almost circular and short, flat voids.

### 2.3.2 Load-Displacement Curves

Figures 2.9 and 2.10 display load-displacement curves for the KKarb C composite. The behavior shown in Figure 2.9, called Type I, was exhibited by the SEN specimens. The linear

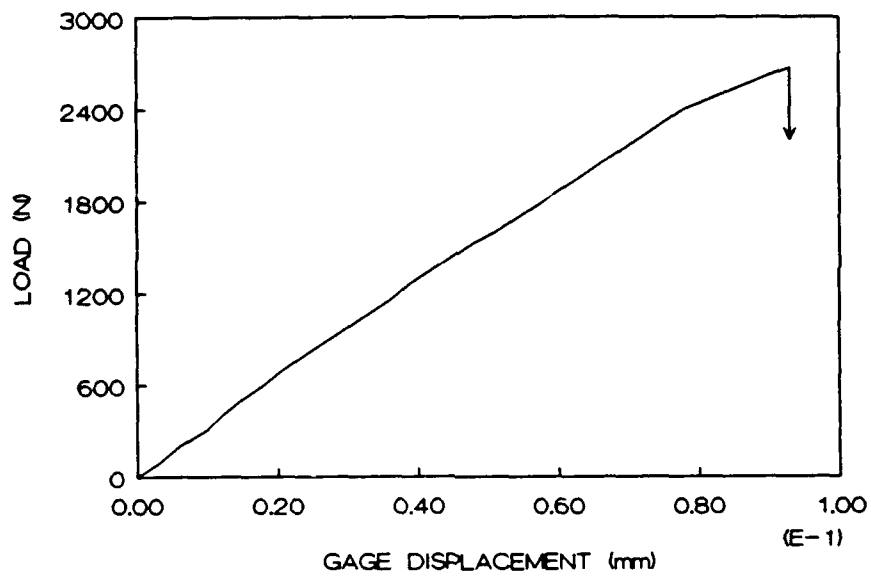


Figure 2.9. Load-displacement curve for KKarb C composite SEN samples.

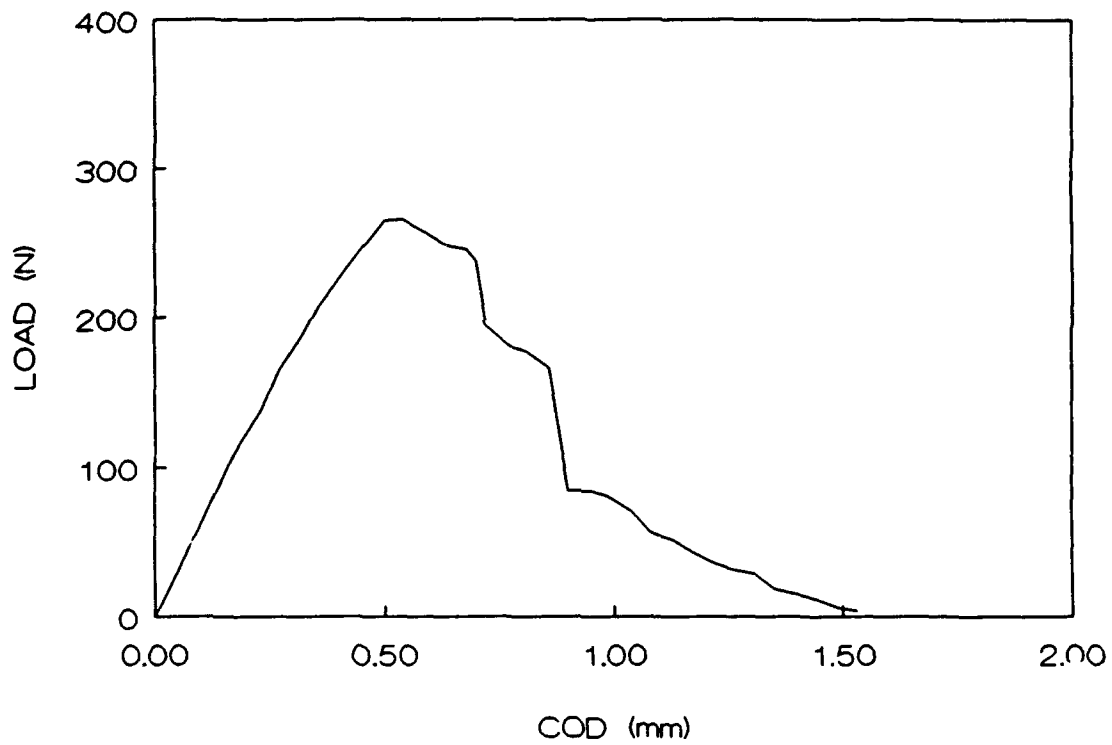


Figure 2.10. Load-displacement curve for KKarb C composite 4PB and CT samples.

portion of the curve is followed by an abrupt load drop as fracture takes place. Type II behavior (Figure 2.10) is characterized by a non-linear region preceding the maximum load and then a stepwise decrease in load with increasing displacement. This behavior was exhibited by both the 4PB and CT samples. The distinction between the former, elastic-like and latter "semi-brittle" behavior is attributed to the load-specimen configuration. SEN specimens experience a tensile load uniformly applied over their width. As soon as the crack front stress reaches a critical value the crack growth proceeds catastrophically through the microcracks parallel to the crack tip and normal to the applied load which leads to an abrupt load drop. In contrast, the CT samples experience tensile and compressive forces. The explanation for the load-displacement curve shape is two-fold. Firstly, C/C composites and fibers possess higher compressive than tensile strengths. The CT specimen is therefore capable of resisting failure to a greater extent than the pure tensile specimen. Secondly, as the stress at each yarn reaches its critical value, the domain adjacent to the crack tip fractures and the load decreases. The decrease in load corresponds to the quicker matrix failure. The load then plateaus until the next domain around the crack front reaches its critical stress level. This process is repeated giving the stepwise behavior seen in Figure 2.10.

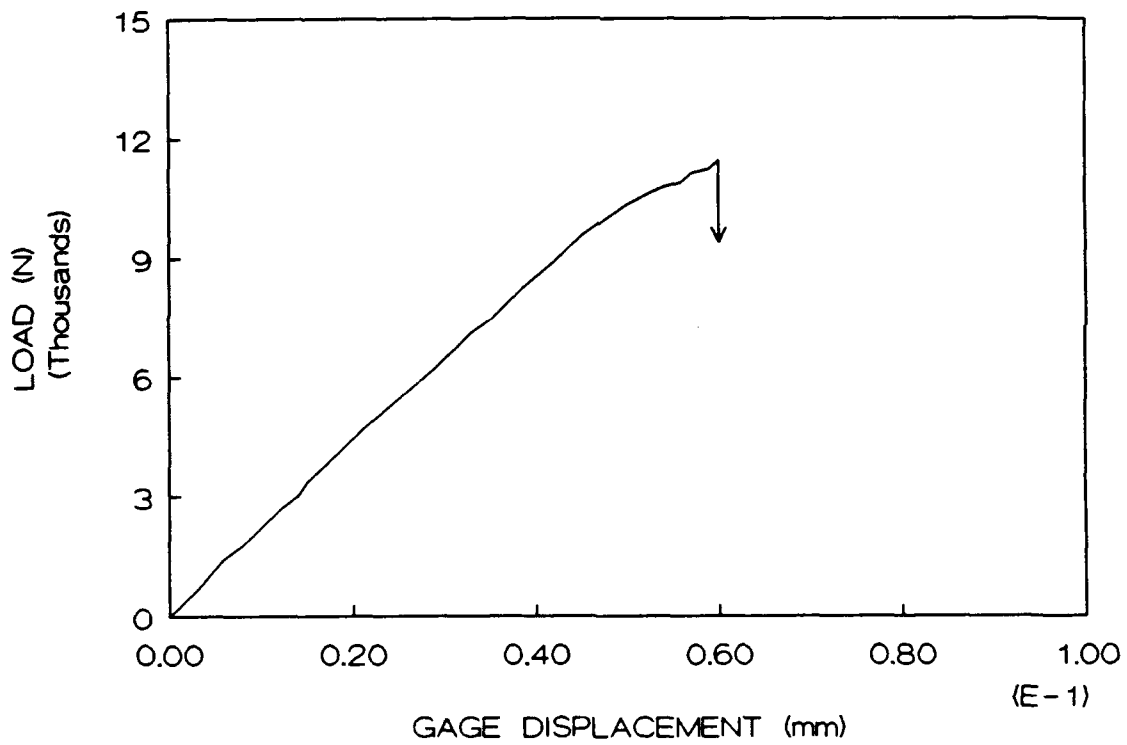


Figure 2.11. Load-displacement curve for T300 HT composite SEN samples.

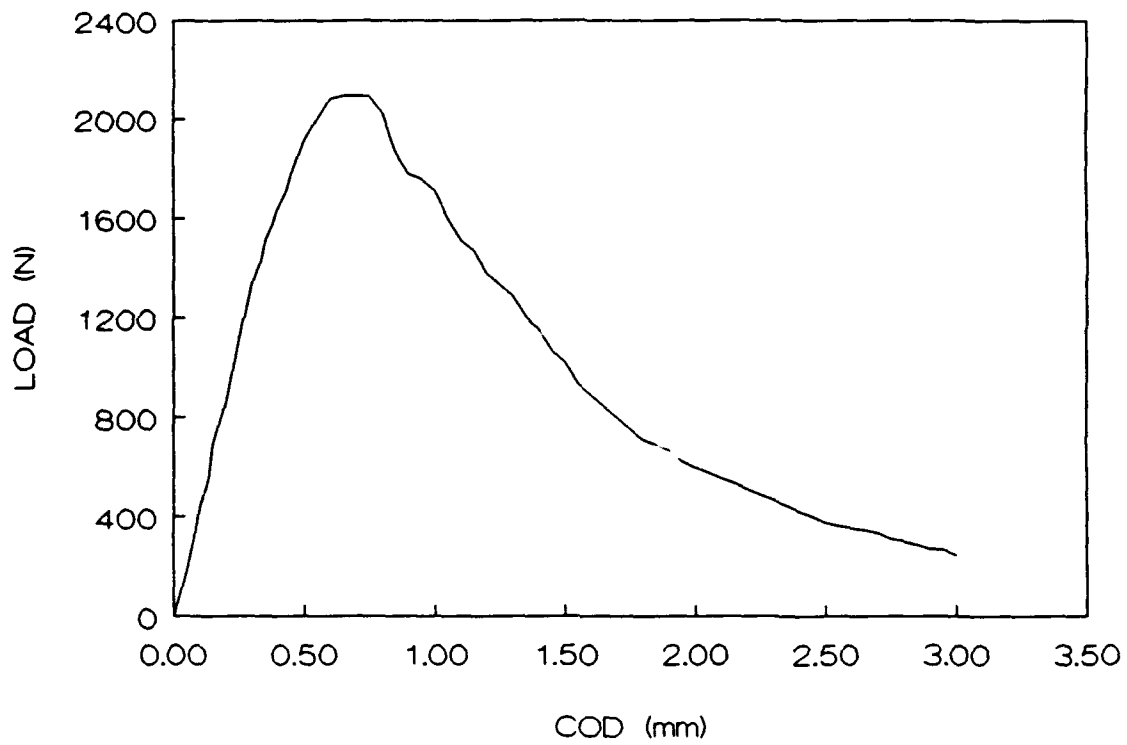


Figure 2.12. Load-displacement curve for T300 HT CT and 4PB samples.

Figures 2.11 and 2.12 are typical load-displacement curves for T300 HT samples. Type I behavior (Figure 2.11), exhibited by SEN samples, is characterized by catastrophic failure preceded by a linear increase in load with displacement. In Figure 2.12 (Type II), the load decreases gradually with displacement after its maximum is reached. Both the 4PB and CT samples exhibited this phenomenon. The maximum loads achieved for the T300 HT samples were greater for every geometry and thickness tested than those of the KKarb C composite. The same explanation for the difference in load-specimen behavior applies to the T300 HT samples.

### 2.3.3 Fracture Toughness

#### 2.3.3.1 LEFM Considerations

The limited non-linearity of the load-displacement curves for both composites suggests the use of  $K_{Ic}$  to characterize the fracture toughness. This parameter is valid if the guidelines set in the ASTM E399 [32] standard are met. In this regard, it is important to note that the guidelines were established for metals and that no standards are available for composites. The fracture behavior of C/C composites contrasts greatly with brittle metals under plane-strain conditions. In 2D C/C composites the crack advances through a heterogeneous field of yarns, matrix and processing flaws. This difference does not necessarily rule out the use of  $K_{max}$ , the maximum stress

intensity factor as a quantitative measure of fracture toughness since linear elastic fracture mechanics (LEFM) are still valid for some composite materials [45-47]. Plane-strain conditions are maintained when the thickness (B) and notch depth (a) exceed certain values:

$$a, B \geq \left( \frac{K_{IC}}{\sigma_y} \right)^2$$

where  $\sigma_y$  is the yield stress. Plane-strain conditions and crack-tip plasticity are however, irrelevant to the fracture behavior of C/C composites. The concept of a plastic zone through which the material is able to deform and resist fracture is not applicable to these materials. A side view of a fractured KKarb C sample (Figure 2.13) showed no increase in the microcrack density which would be associated with a damage zone. Therefore, the size requirements dictated by the ASTM standard are inconsequential and the fracture processes at the crack tip will not be affected by deviations.

It is also required to ascertain whether subcritical crack propagation has been suppressed prior to critical crack propagation. The 95% secant criterion has been applied. A candidate load  $P_0$  is obtained from a secant drawn with a slope equal to 95% of the linear portion of the load-displacement curve. The maximum load ( $P_{max}$ ) is then compared to the candidate load. If the ratio,  $P_{max}/P_0$  is less than or equal to



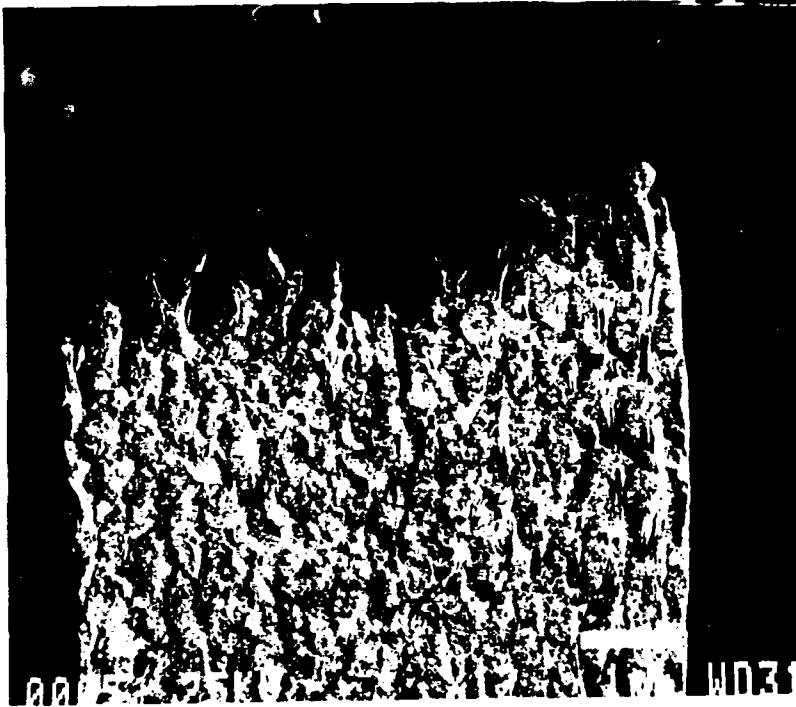


Figure 2.13. End view of 4PB KKarb C composite.

1.1 then the magnitude of subcritical crack propagation is negligible. In the case of the KKarb C composite, the ratio was less than or equal to 1.1 for all cases. The ratio for the T300 HT composite varied from 1.1 to 1.4 indicating that the criterion is not far from validity for the T300 HT material.

Lastly, crack propagation should occur within the notch plane. However, the crack grew both above and below the notch plane due to the ability of the fibers and microstructural flaws to deflect the crack path. Since not every criterion required for the use of ASTM  $K_{Ic}$  has been satisfied the maximum load was taken in the evaluation of the fracture toughness and the effects of non-linearity in some of the load-displacement curves ignored.

#### 2.3.3.2 $K_{max}$

##### a) KKarb C Composite

Average  $K_{max}$  values obtained for KKarb C are shown in Table 2.3. As seen, neither the specimen configuration nor the thickness had a significant influence on fracture toughness. Hence, the plane-stress/plane-strain transition as a function of specimen thickness in monolithic materials is absent. Again it is noted that material heterogeneity is the source of the increased toughness over the constituents rather than crack-tip plasticity.

Table 2.3  
 $K_c$  for KKarb C Composite

Thickness (mm)	$K_c$ (MPa*m <sup>1/2</sup> )		
	4PB	CT	SEN
6.5	5.4	5.6	---
3.0	---	5.2	6.3
1.5	---	---	5.1

The warp and fill directions were unknown for the T300 HT composite and any effects imposed by the associated yarn density variations would have to be accounted for in subsequent characterization. Therefore, four-point bend specimens were cut and tested in two directions arbitrarily assigned the designations X and Y. The notch was cut in one plane and also in a plane perpendicular to this one. The  $K_{max}$  values (Table 2.4) for these samples display a small dependence on notch direction since the values are within an acceptable variance. Therefore, subsequent testing was done only in the direction assigned Y.

b) T300 HT Composite

Table 2.5 lists the average  $K_{max}$  values for the T300 HT samples. The 4PB and CT results show no significant variance with specimen thickness or configuration. However, for an identical sample thickness, the SEN  $K_{max}$  ( $26.7 \text{ MPa}\cdot\text{m}^{1/2}$ ) is almost two times that of the CT sample  $K_{max}$  ( $14.3 \text{ MPa}\cdot\text{m}^{1/2}$ ). The variation is a reflection of the interaction between the stress field and the hierarchical construction of fibers, matrix, and microstructural flaws. In the CT geometry, the stress state is a combination of tensile and compressive forces. As the crack advances across the sample the crack front stress changes from tensile to compressive. The crack under a compressive stress perceives only the microdefect field directly at the notch tip. The SEN configuration in

Table 2.4  
 $K_c$  for T300 HT  
X and Y Directions

Direction	$K_c$ (MPa*m <sup>1/2</sup> )
X	17.5
	17.0
Y	15.9
	15.4

Table 2.5  
 $K_c$  for T300 HT Composite

Thickness (mm)	$K_c$ (MPa*m <sup>1/2</sup> )		
	4PB	CT	SEN
6.5	18.2	16.5	--
3.0	--	14.3	26.7
1.5	--	--	24.7

contrast, is one of pure tensile loading over the bulk of the specimen. The crack is guided simultaneously by the microcracks and voids. Propagation occurs as the crack tip seeks flaws through which it may advance either through the bundles (microcracks) or along the perpendicular plies (voids). The crack front moves in a stepwise manner through the voids and then a microcrack as fracture parallel to the notch occurs. Fracture of yarns perpendicular to the crack tip must take place for the crack to proceed across the sample width.

The further elucidation of the relationship between the load-displacement curves,  $K_{max}$ , and the composite microstructure required examination of the fracture surfaces. The type of fracture mechanism and its relative degree of occurrence for a particular geometry and composite are related to the calculated fracture toughness values. Additionally, since the type and location of flaws in the unfractured materials has been identified, preferential crack propagation in these areas would support the assumption that microstructural defects act to increase the toughness by guiding the crack growth.

#### 2.3.4 Mechanistic Analysis

It is again be emphasized that the two materials vary in fiber and matrix materials and weave design. The rayon fibers

of the KKarb C composite are weaker than the PAN fibers of the T300 HT material. Moreover, since pitch is able to form a mesophase and is hence, highly graphitizable, it is expected that it will be stronger than the phenolic resin matrix of the KKarb C composite.

#### 2.3.4.1 KKarb C Composite

The macroscopic appearances of the KKarb C 4PB, CT and SEN samples were very similar in that the crack propagated along a plane at approximately a 15° angle to the notch plane. Moreover, the crack did not deviate from this plane once propagation had begun. Therefore, a representative sample from the entire set was chosen. Figure 2.14 shows an overview of a KKarb C compact-tension sample at a 6.5 mm thickness. The fracture surface shows events occurring parallel and normal to the fracture surface. Mechanisms normal (Figure 2.15) to the fracture surface include: 1) yarn fracture (arrow Y), 2) fiber pullout (arrow P) which leaves a crenulated hole characteristic of rayon fibers, and 3) delamination of the yarn from the matrix (Figure 2.16, arrow D). On the outer edges of the bundle in Figure 2.16 are skeleton-type areas where fibers were pulled away from the yarn leaving only the matrix which surrounded the fibers. Within the matrix material (arrow M) in the upper region of the photograph is a microcrack extending from one bundle to another. The crack runs circumferentially around the bundle as a result of the





Figure 2.14. Overview of 6.5 mm thick compact-tension KKarb C composite.

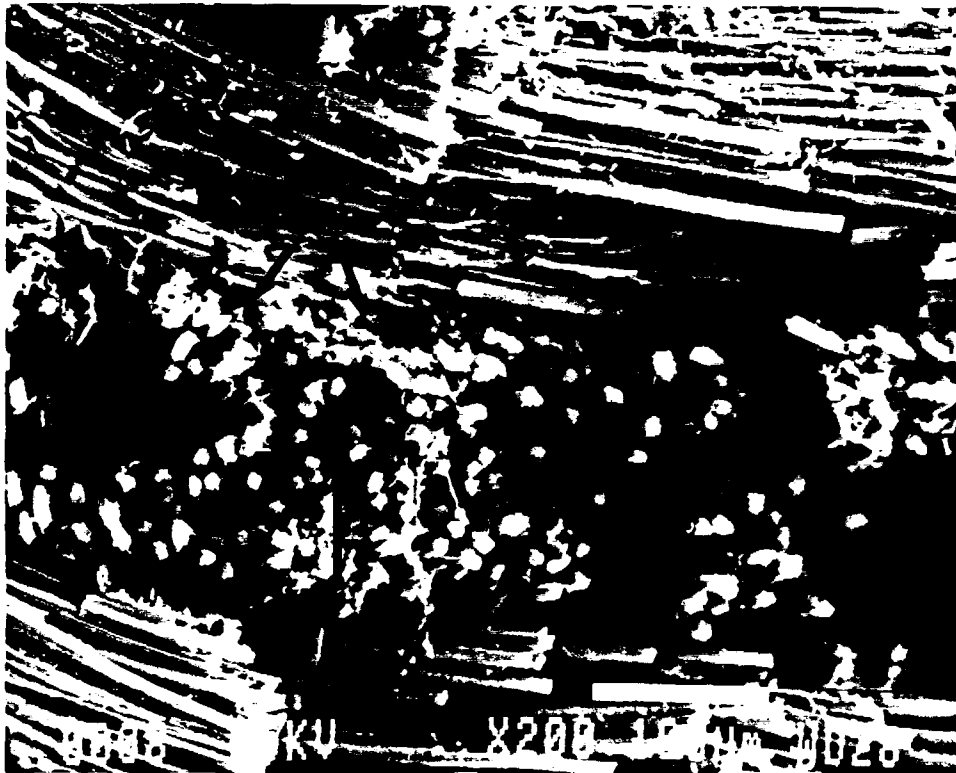


Figure 2.15. SEM micrograph of KKarb C composite showing yarn fracture (arrow Y) and fiber pullout (arrow P) perpendicular to mean crack path.



Figure 2.16. SEM micrograph of KKarb C composite showing delamination (arrow D) perpendicular to mean crack path and matrix failure (arrow M).

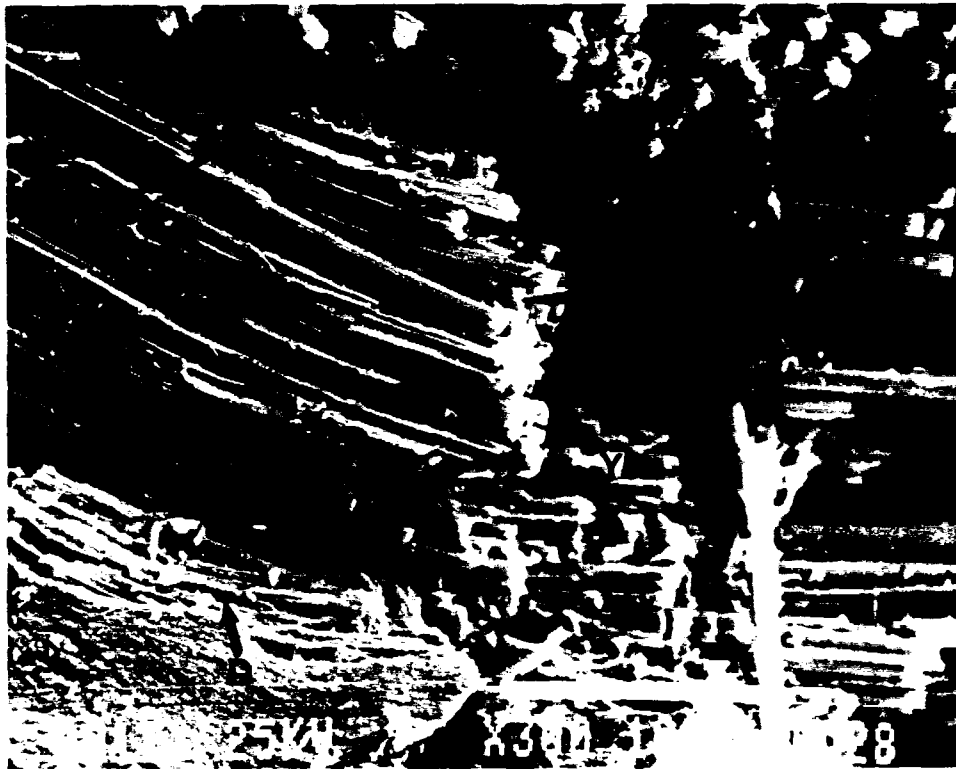


Figure 2.17. SEM micrograph of KKarb C composite showing fiber fracture (arrow F), yarn fracture (arrow Y), and delamination (arrow D) parallel to mean crack path.

low interfacial shear strength.

Figure 2.17 indicates the variety of mechanisms occurring parallel to the fracture surface: 1) fiber fracture (arrow F) within the yarn which necessarily precedes bulk yarn fracture (arrow Y), and 2) delamination evidenced by the smooth fracture surfaces (arrow D).

The mechanistic analysis leads to the conclusion that the load-displacement behavior in the CT and SEN samples is a function of the stress state. The slanted appearance of the fracture surface may be explained by the regular occurrence of microcracks parallel to the crack tip. The yarns deflect the crack tip along the fiber/matrix interface until another microcrack is reached. Since the microcracks are regularly spaced the distance the crack must proceed before encountering another microcrack is relatively short. The fact that the crack preferentially propagates below or above the notch plane once initiation takes place is due to the localized stress concentration at the notch tip coupled with the adjacent plane of microcracks.

Lastly, the lack of one dominant fracture mechanism in either the CT or SEN configuration naturally precludes the assignment of one particular mechanism which increases the fracture toughness. The sum of the fracture energies of the described mechanisms determines the fracture toughness. The relative contribution of each mechanism depends upon the

specific mechanism fracture energy. Since the type and relative amount of each pre-fracture mechanism is the same for the 4PB, CT and SEN load-specimen configurations, the  $K_{max}$  value obtained is valid for all thicknesses and geometries tested.

#### 2.3.4.2 T300 HT Composite

Both a CT and SEN sample of the T300 HT composite were examined microscopically because of their radically different fracture surfaces. Figure 2.18 is a macroscopic overview of the CT sample fracture surface. Apparent are two regions, labelled 'S' for "shaggy" and 'F' for "flat" which differ in their dominant fracture mechanisms and brightness. Region S is darker and protrudes further above the notch plane than Region F. Examination of Region S shows yarn fracture in a perpendicular direction (Figure 2.19, arrow Y). The lighter appearance of the perpendicular yarn bundles evidences the degree of protrusion above the mean crack path. Yarn fracture also occurred below the notch plane in the darker regions. The presence of yarn failure both above and below the mean crack path may be explained by considering the individual fibers. The fiber strength is dictated by the presence of microstructural flaws along the longitudinal axis. A discontinuity will act as a stress concentrator and cause fiber breakage. Since the distribution of flaws is random yarn failure above and below the mean crack path are equally

Region S

Region F



Notch  
--->

2 mm

Figure 2.18. Overview of 6.5 mm thick compact-tension T300 HT composite which illustrates the two regions of failure, Regions S and F.

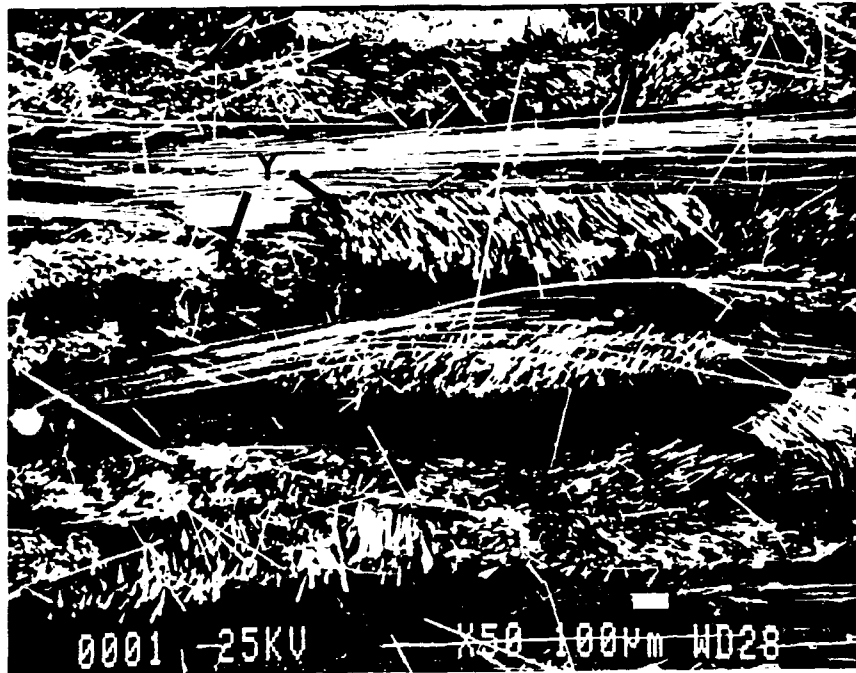


Figure 2.19. SEM micrograph taken in Region S illustrating yarn fracture above and below the mean crack path (arrow Y).





Figure 2.20. SEM micrograph taken in Region F illustrating yarn and fiber fracture (arrows Y and F, respectively) parallel to the mean crack path.

probable.

Region F begins where the sample extends laterally under the action of the dominant compressive stress. In comparison to Region S where yarn fracture occurred in the perpendicular direction, yarn and fiber fracture in Region F occurred primarily in the parallel direction (Figure 2.20, arrows Y and F). This is again due to the compressive stress acting to push the fracture surfaces together. Figure 2.21 shows fiber fracture (arrow F) perpendicular to the surface in Region F but the degree of pullout (arrow P) is considerably smaller than in Region S. Fiber debonding and pullout are more likely in tension where only the low interfacial shear stress must be overcome and the surfaces are not constricted as in mixed loading. Fibers experiencing a compressive stress fail by buckling at the level of bulk yarn fracture. The appearance of the fractured yarns in Figure 2.21 is therefore a result of the compressive stress.

Interesting to note in Figure 2.22 is the lamellar graphitic structure between the laminates. The presence of a sheath structure suggests that the mesophase pitch and was oriented such that the basal planes of the graphite lay perpendicular to the surrounding fibers. When the basal planes of fibers are oriented in such a way, the fibers have higher tensile strengths and it is suggested that a matrix oriented in a similar fashion is also stronger. Matrix

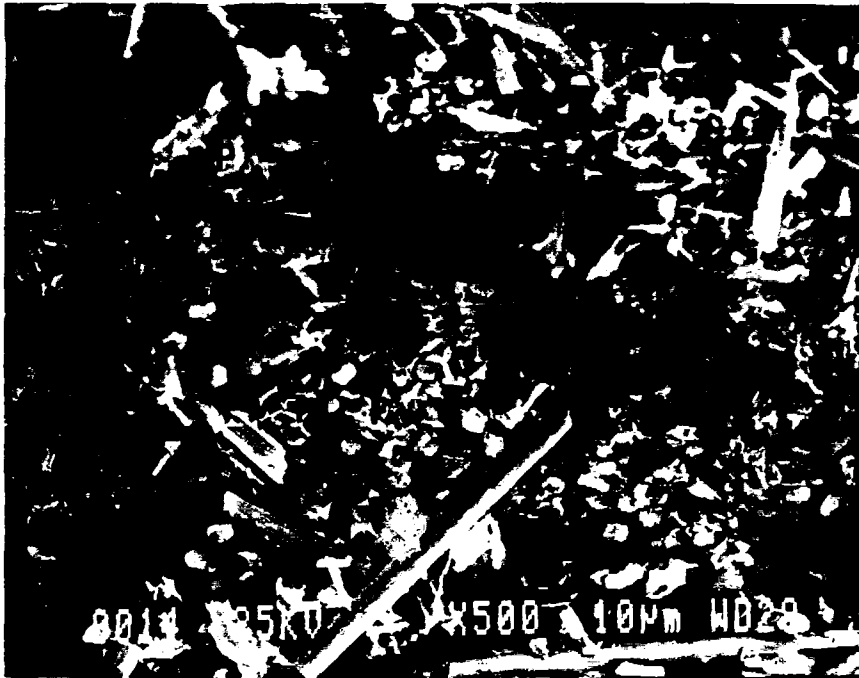


Figure 2.21. SEM micrograph taken in Region F showing fiber fracture (arrow F) and pullout (arrow P) perpendicular to mean crack path.

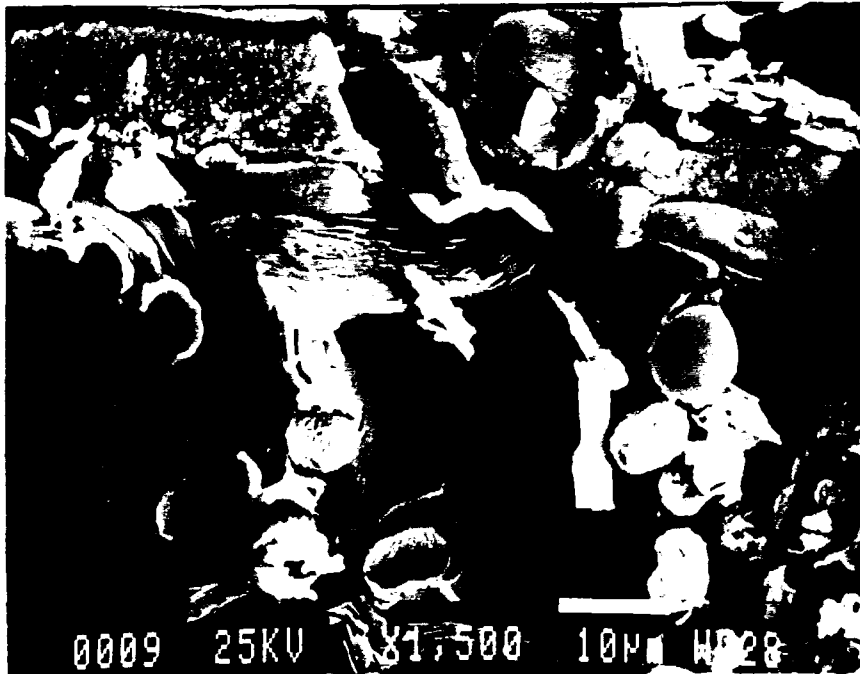


Figure 2.22. SEM micrograph taken in Region F showing matrix failure and the development of a graphitic structure.

failure in the pitch varies considerably with that seen in the phenolic resin (Figure 2.17). The contribution of the stronger matrix to the fracture behavior is apparent from the higher  $K_{max}$  values of the T300 HT composite.

Examination of the crack path of a T300 HT SEN sample (Figure 2.23) revealed two primary differences from the CT sample. Firstly, there was no evidence of sample buckling and secondly the height of the fractured yarns above the mean crack path ranged between 5-6 mm as compared to 2-3 mm for the CT sample in Region S. The combined action of compressive and tensile stresses hinders the development of an active zone. The resulting active zone size is then 10-12 mm for the SEN samples but only 4-6 mm for the CT samples. The size difference corresponds to the variation in  $K_{max}$  values (Table 2.5).

The KKarb C composite did not exhibit the variation in fracture behavior seen in the T300 HT samples as a result of the microdefect field. The population of microcracks is much higher in the KKarb C (2165 per  $\text{cm}^2$ ) than in the T300 HT composite (375 per  $\text{cm}^2$ ). Therefore the crack which proceeds through the microcracks to the next yarn must not travel as far before encountering another microcrack (Figure 2.24). Yarn fracture perpendicular to the mean crack path does not occur above or below the plane but rather in the plane. The lower microcrack density of the T300 HT composite necessitates



Notch  
--->

2 mm

Figure 2.23. Overview of T300 HT SEN sample at a thickness of 3 mm.

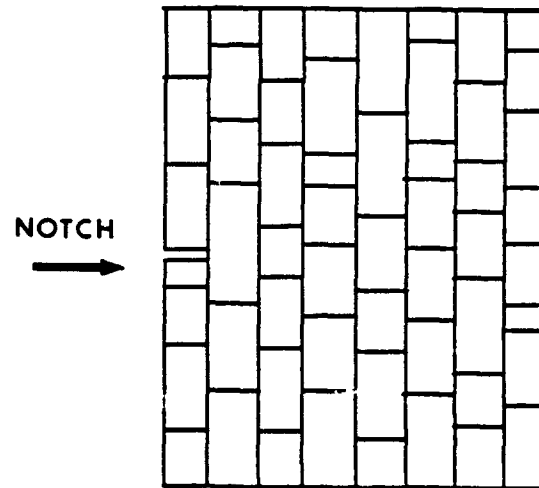


Figure 2.24. Schematic of KKarb C composite showing the distribution of microcracks.

extensive crack growth through the voids and perpendicular to the mean crack path in order to find a microcrack and initiate yarn fracture.

#### 2.4 CONCLUSIONS

A description of the fracture behavior of two C/C composites differing in weave type as well as fiber and matrix precursors was given. The materials were tested in 4PB, SEN, and CT configurations to determine  $K_{max}$  and its dependence on thickness and test geometry. The fracture surfaces were examined to qualitatively assess the mechanisms influencing the fracture behavior. The following conclusions are presented:

- 1) The average  $K_{max}$  for the KKarb C composite was  $5.4 \text{ MPa}\cdot\text{m}^{1/2}$  and was independent of configuration and thickness. The latter result occurs with C/C composites in which material flaws rather than crack-tip plasticity are the toughening mechanisms.
- 2) The T300 HT composite displayed a geometry dependence but was independent of thickness within one configuration. The  $K_{max}$  value of the SEN samples ( $26.7 \text{ MPa}\cdot\text{m}^{1/2}$ ) was approximately two times greater than that of the CT samples ( $14.3 \text{ MPa}\cdot\text{m}^{1/2}$ ) of the same thickness. This phenomenon has been attributed to the stress state and its interaction with the microflaws.
- 3) Deviation of the fracture path from linearity occurred as



the crack tip encountered a microdefect. Because the KKarb C composite contained only microcracks in the notch plane the crack advanced collinearly and the resulting fracture toughness was lower than in the T300 HT composite.

4) The macroscopic and microscopic fracture surfaces of the samples provided an explanation for the higher fracture toughness values obtained for the T300 HT compared to the KKarb C. Namely, the T300 HT composite displayed a larger active zone containing more yarn fracture and fiber pullout normal to the notch plane than the KKarb C composite which resulted in  $K_{max}$  values 3 to 4 times higher. In this respect the influence of microvoids on the toughness of a composite is apparent. If fracture is to proceed above the notch plane then a lower energy region such as a microvoid must exist. Further propagation occurs only after yarn fracture has taken place through a microcrack. Since the microcrack population is lower in the T300 HT composite the crack front must advance further before encountering a microcrack.

### 3.1 INTRODUCTION

Three-dimensional carbon-carbon composites (3D C/C) are emerging as an important class of materials which are unique among C/C composites in their ability to be tailored for specific applications. The repeated impregnation cycles and high temperatures incurred during carbonization and graphitization cause the formation of a heterogeneous microstructure consisting of cracks and voids. A study was done on the interaction between the microdefect field and fatigue behavior [50]. The crack was found to propagate into processing-induced microvoids away from the fiber-matrix interface where failure had initiated. Characterization of the material behavior in tension and flexure [27] showed that the tensile and flexural strengths were a function of fiber density as well as gaps and cracks around the yarns.

The fracture toughness of a 3D composite has been determined by calculating  $G_c$  from  $K_c$  [39,40]. The latter studies have not examined the influence of the microstructure on the fracture behavior. The results showed that  $G_c$  varied from 3-8 J/m<sup>2</sup> and that the fracture path was tortuous and not predictable. In this chapter  $K_{max}$ , the fracture toughness calculated from the maximum load, is used to describe the interplay of the microstructural hierarchy and the fracture behavior. The form of the 3D material supplied for this study allowed the effects of notch orientation and depth to be

simultaneously examined. The  $K_{\max}$  values obtained were related to the microstructure and fracture surface appearance, and load-displacement behavior.

### 3.2 EXPERIMENTAL

#### 3.2.1 Material and Test Description

A portion of the original billet received from Edwards Air Force Base is shown in Figure 3.1. For convenience the yarn directions are labelled 'R' for radial, 'C' for circumferential, and 'A' for axial. The distance between the radial yarns increases from 4.1 mm at the inner radius to 4.5 mm at the outer radius. The fiber center-to-center spacing for the axial and circumferential yarns is 1.5 mm.

Originally a compact tension specimen was machined to measure  $K_{\max}$ . Despite reinforcement at the load points however, the specimen failed at the grips. Therefore the three-point bend geometry (3PB) was chosen. A slab was sliced from the billet in the radial direction from which the 3PB specimens were cut. The dimensions (Figure 3.2) gave a span-to-width ratio of four. Each specimen was then notched using a 0.25 mm diamond-edged saw and sharpened with a razor blade to its test depth. The three a/W ratios chosen were 0.2, 0.3, and 0.5. The number of samples at each notch depth and orientation are listed in Table 3.1. It is noted that twelve samples were tested in the radial direction at an a/W of 0.2.

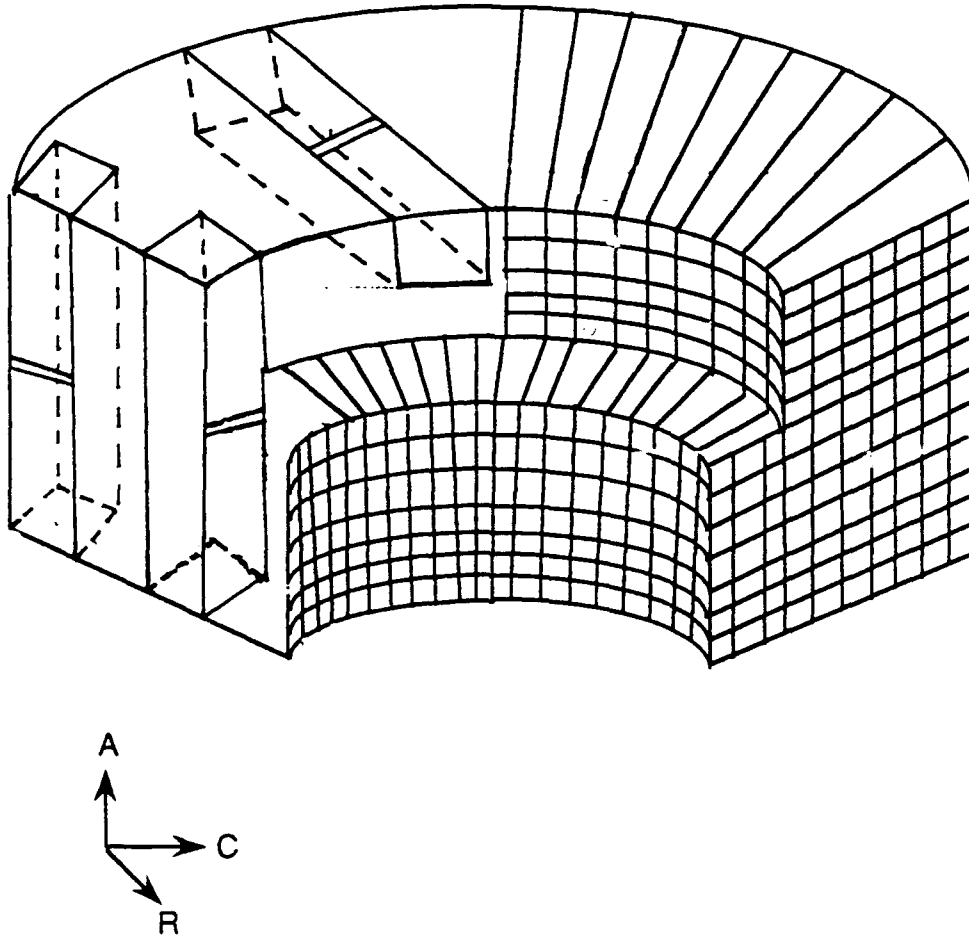
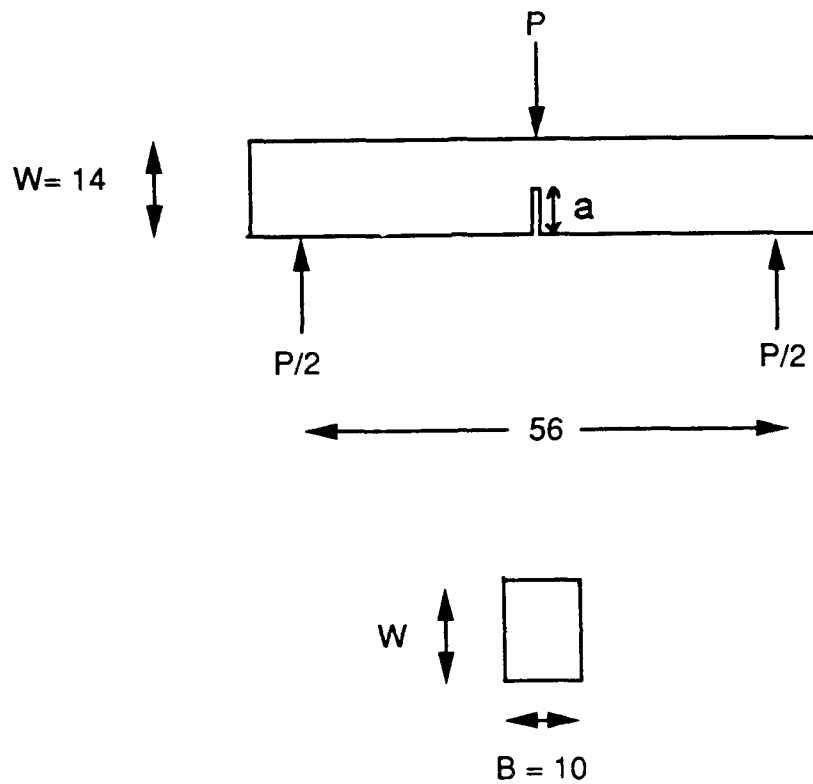


Figure 3.1. A portion of the original 3D billet from which the 3PB specimens were cut. The distance between the radial yarns increases from 4.1 mm at the inner radius to 4.5 mm at the outer radius.



All Dimensions in Millimeters

Figure 3.2. Three-point bend geometry where  $S$  is the span,  $W$  the width,  $B$  the depth and  $a$  the initial notch depth.

The motivation for this choice will be explained in the results section of the chapter. The tests were conducted under monotonic loading and displacement control in an MTS apparatus at room temperature at a crosshead speed of 0.25 mm/min. The load, load-point displacement (LPD) and crack-opening displacement (COD) were monitored during the test. A COD gauge was mounted around the crack mouth using knife edges equidistant from the notch edges.

A 25 x 10 mm sample was cut from each of the three mutually perpendicular planes of the unfractured material and mounted in polyester resin. The mounted samples were polished using 300 grit SiC paper followed by 600 grit and 30  $\mu$ m lap paper and viewed in an optical microscope under direct lighting. Additional optical micrographs were taken of the fracture path in order to assess the degree of diffusivity associated with notch length and orientation. Lastly, higher magnification details of the fracture mechanisms were observed employing a JEOL 35CF scanning electron microscope. The fracture surfaces were either gold or palladium sputter-coated before examination.

The stress-intensity factor was computed from [32]:

$$K_c = \frac{P_{\max} S}{BW^{3/2}} f(a/W)$$

where  $P_{\max}$  is the maximum load, S the distance between load

Table 3.1  
3D Test Samples

Notch Orientation	a/W	No. of Samples
R	0.2	12
	0.3	3
	0.5	3
C	0.2	3
	0.3	3
	0.5	3
A	0.2	2
	0.3	2
	0.5	3

points, B the specimen thickness and W the specimen width.

The geometric correction factor  $f(a/W)$  was [44]:

$$f(a/W) = \frac{2}{\pi} \frac{[1.99 - a/W(1-a/W)(2.15 - 3.93(a/W) + 2.7(a/W)^2)]}{(1 - 2(a/W))(1 - a/W)^{3/2}}$$

### 3.3 RESULTS AND DISCUSSION

#### 3.3.1 Microstructure

The composite in Figure 3.1 has orthotropic character due to the architectural heterogeneity consisting of yarns and matrix and processing-induced microflaws. The fracture behavior is dictated by the constituents, microstructure and the imposed stress state. Therefore, an examination of the unfractured material was performed to elucidate the effects of yarn density and microflaws on  $K_{max}$ . The samples cut from the unfractured 3D billet are pictured in Figures 3.3, 3.4, and 3.5. The cross-sectional area of yarns encountered by the propagating crack per unit area was determined from a 4 mm<sup>2</sup> area on the optical micrographs. In both the radial and circumferential notching directions a greater area of cross yarns is encountered than in the axial direction (Table 3.2). In Figure 3.3 the cut was made so that the radial and axial (R and A) fibers are in the plane of the micrograph and the circumferential (C) fibers protrude from the plane. This cut corresponds to the plane into which a circumferentially-



Table 3.2  
Yarn Cross Section per Unit Cross Section  
at Crack Front

---

Sample	YCS/UCS
R-A	2.2
R-C	1.7
C-A	0.4

---



---

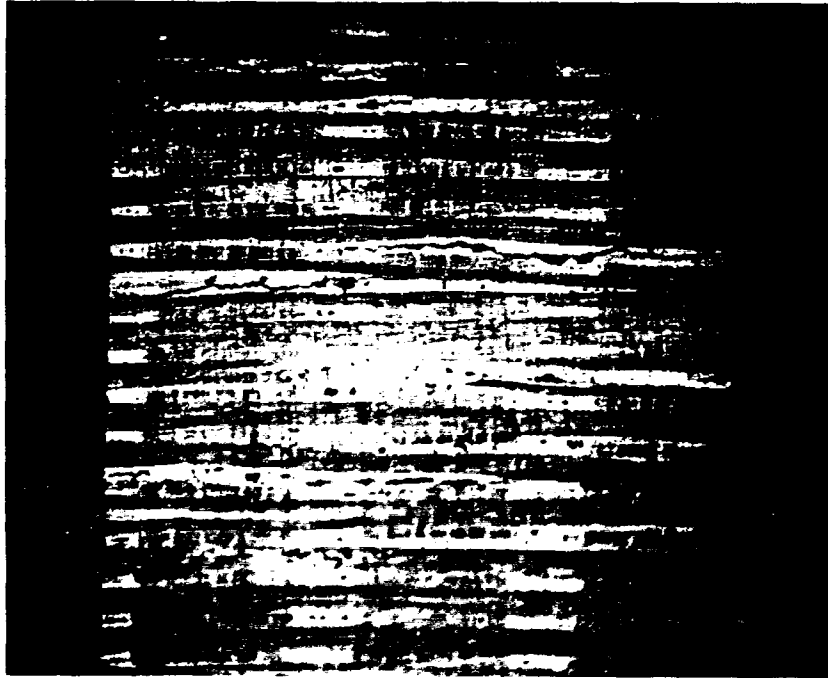
2 mm

Figure 3.3. Optical micrograph of the unfractured material cut along the radial-axial plane. The circumferential yarns protrude from the sample surface.

notched sample propagates. Microcracks extend along the axial yarns through the sample thickness every four to five yarns. The microcracks are contained within matrix material and are connected periodically by voids (darker, circular regions) on the radial yarns. The cracks are discontinuous and do not extend along the full length of a yarn. It is also noted that the axial yarns surrounding both the smaller and larger microcracks are distorted. The waviness of the axial yarns may be ascribed either to plastic deformation incurred during high temperature heating [25] or to the material attempting to accommodate the additional strain imposed by the thermal expansion differential.

Figure 3.4 depicts the sample surface along the R-C plane. The circumferential yarns are horizontal and the radial yarns vertical in this micrograph. The samples notched in the radial direction fractured along this plane. Cracks and voiding along the circumferential yarns can be attributed to either material loss through thermal cycling shrinkage or to gas bubbles trapped within the matrix upon cooldown [25]. Therefore, ellipsoidal voids at the R-C crossover points may be indicative of the presence of gas pores. The voids in this plane are larger than those in Figure 3.3.

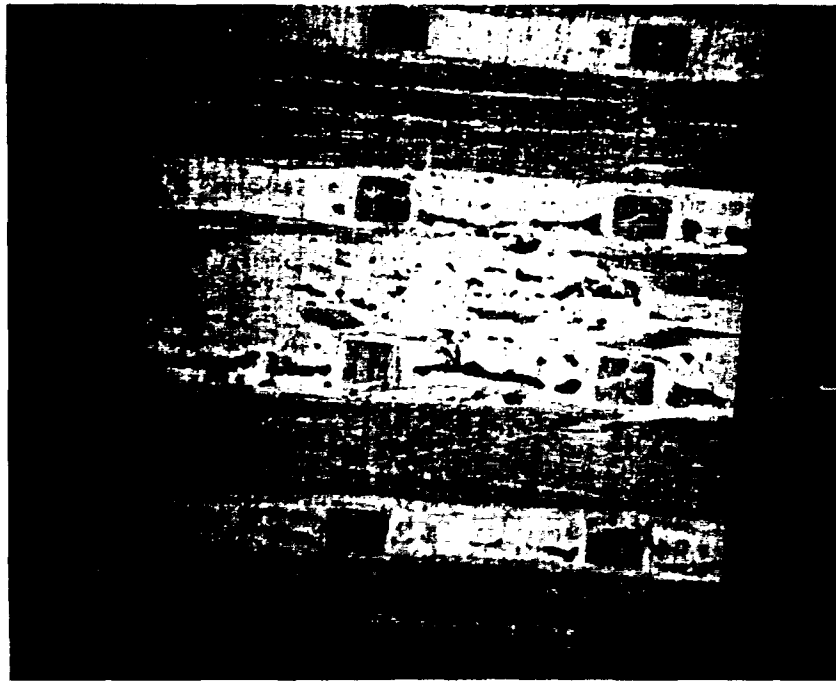
The sample from the C-A plane is shown in Figure 3.5. This last specimen corresponds to the plane along which samples notched in the axial direction fractured. When the



---

2 mm

Figure 3.4. Optical micrograph of the unfractured material cut along the radial-circumferential plane. The axial yarns protrude from the sample surface.



---

2 mm

Figure 3.5. Optical micrograph of the unfractured material cut along the circumferential-axial plane. The radial yarns protrude from the sample surface.

initial polishing was done the axial fibers appeared smeared and it became difficult to resolve both yarns simultaneously. Therefore this micrograph shows only the circumferential yarns in the horizontal direction and the radial yarns out of the plane. The axial yarns extend vertically behind the circumferential yarns. It is expected that the resistance to fracture will be less than that in the other directions since the area of cross yarns is significantly less than in the radially and circumferentially-notched samples (Table 3.2). This plane also contained the largest voids of the three planes which promote preferential crack propagation along the circumferential-axial yarn interface. Figure 3.5 also shows small cracks extending around the radial yarns between the voided areas on either side of the yarn. The cracks result from the greater thermal expansion of the composite in the radial and circumferential directions compared to the transverse expansion of the circumferential bundles. Compressive stresses are therefore induced in the circumferential yarns. Upon cooldown the situation is reversed and cracks form within the matrix to relieve the residual tensile stresses [24].

### 3.3.2 Fracture Toughness as a Function of Notch Orientation

The influence of the microstructure particularly the architecture of the yarns and matrix on the crack resistance

was examined as a function of notch direction and depth. Methods to obtain the fracture toughness such as  $J_{Ic}$  and the compliance-calibration technique contain difficulties. In the former the determination of a crack extension is practically impossible because the assignment of a distinct crack tip is limited by the material morphology. The compliance method used to yield  $G_{Ic}$  assumes that a change in stiffness is due to an increase in crack length. However, the current research showed that this was not necessarily true. The decrease in compliance is instead a result of the interaction of the microflaws with the applied stress. The use of  $K_{max}$  to characterize the fracture behavior versus  $K_{Ic}$  has been justified for the 2D composites (see previous chapter). It was concluded that the lack of crack-tip plasticity and collinear crack propagation associated with composite materials invalidated the use of  $K_{Ic}$  as a measure of the onset of critical crack propagation. Therefore, the fracture toughness is best measured employing  $K_{max}$  although it is acknowledged that more advanced models need to be implemented which incorporate the nature of the fracture process.

#### 3.3.2.1 $K_{max}$ Values

The  $K_{max}$  values for each of the orientations and depths are displayed in Table 3.3. Discontinuities were ignored in the calculation of  $K_{max}$ . The circumferential samples for all

Table 3.3  
 $K_c$  Values for 3D Composite

Orientation	a/W	$K_c$ (MPa*m <sup>1/2</sup> )
R	0.2	5.2±0.6
C		7.8±1.3
A		1.9
R	0.3	3.8±0.4
C		5.6±0.2
A		1.9
R	0.5	3.2±0.7
C		4.8±1.0
A		1.7±0.6



notch depths tested had the highest  $K_{max}$  values. In comparison, the axial sample  $K_{max}$  was approximately one-fourth that of the circumferential samples at an  $a/W$  of 0.2 and was independent of notch depth. Referring back to Figures 3.3, 3.4, and 3.5 it becomes clear that the higher  $K_{max}$  value was derived from the greater yarn density encountered at the crack front coupled with the lower microflaw population and size. The axially-notched sample has a continuous network of large microvoids surrounding the yarns (Figure 3.5) which serve to provide an easy path for crack growth.

The fundamental aspects of the fracture processes are reflected in the load-displacement shape. For each orientation the curve, fracture path, and surface mechanisms are further examined to explain the influence of the microstructure hierarchy on the  $K_{max}$  values.

#### 3.3.2.2 Load-Displacement Curves and Mechanistic Analysis

Figure 3.6 is a load-displacement curve for a notch in the circumferential direction at an  $a/W$  of 0.2. The curve remains linear until  $P_{max}$  due to the stiffness of the circumferential fibers. The compliance of the material reflects the resistance of the unnotched ligaments to failure. Since the yarns are woven at an angle to the notch tip they are less compliant than the radial yarns under uniform stress. Additionally, all three circumferential samples showed less

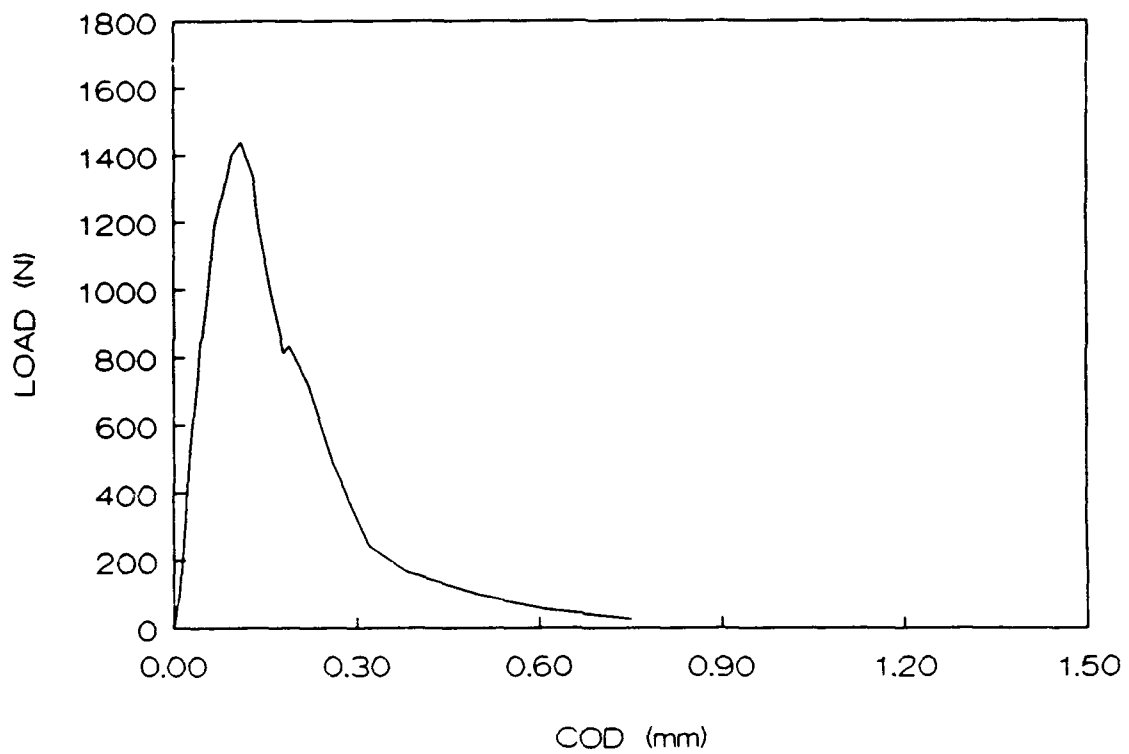


Figure 3.6. Load-displacement curve for a circumferentially-notched sample at an  $a/W$  of 0.2.

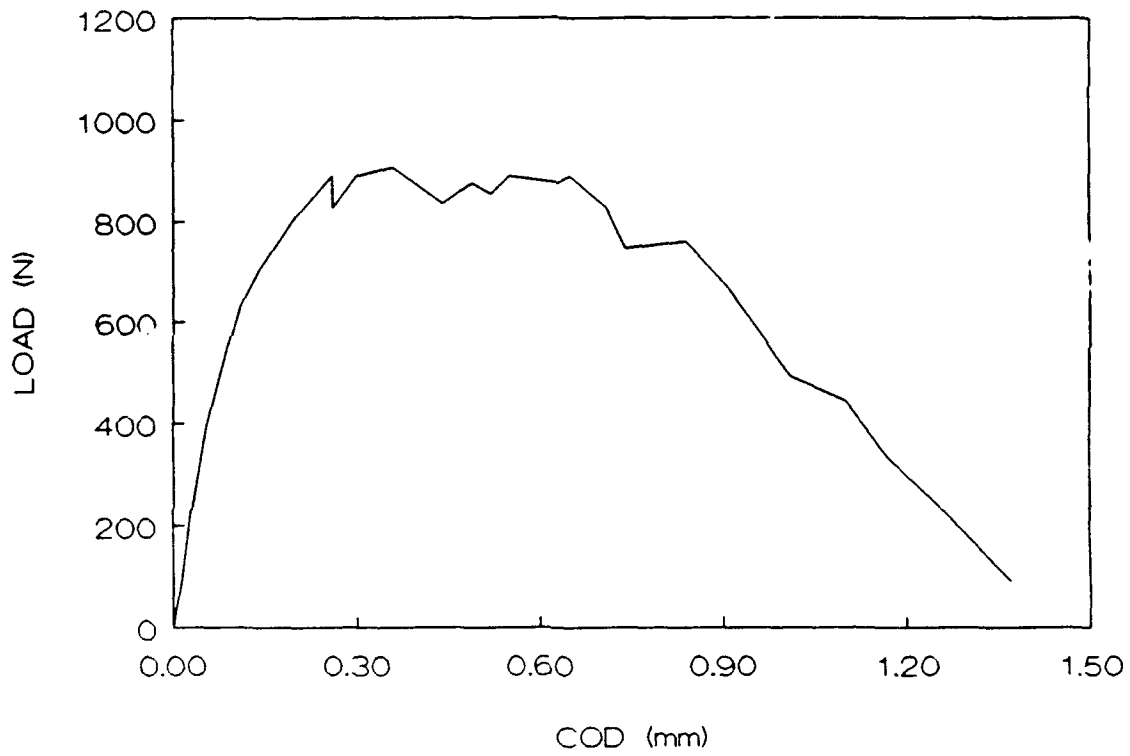


Figure 3.7. Load-displacement curve for a radially-notched sample at an  $a/W$  of 0.2.

variability in the load-displacement curve shape and fewer fluctuations in  $P_{max}$  than would be seen within a random set of radially-notched samples. The steady load decrease reflects the ability of the specimen to resist catastrophic failure due to the compressive stress and interdigitated yarns.

The load versus COD curve for a radially-notched sample at an  $a/W$  of 0.2 is shown in Figure 3.7. Since the radial yarn spacing increased from the inner to outer radius the difference in yarn density might have had an effect on the crack initiation resistance. Therefore, twelve specimens at this notch depth were tested. The results indicated however, that the maximum load was independent of specimen location and it was decided that three specimens were sufficient. In general the load-displacement curves exhibited three characteristics: 1) a linear climb to approximately one-half  $P_{max}$ , 2) a non-linear climb to  $P_{max}$  accompanied by pop-ins, and 3) stable crack growth following  $P_{max}$ . The primary difference between the radial and circumferential orientations is the initial sharp rise for the circumferentially-notched samples. Discontinuities such as pop-ins are generally attributed to matrix cracking although such behavior should not be assumed from the present study. The last feature varied among the samples in that steady fracture could occur around  $P_{max}$  or at loads one-third to one-half  $P_{max}$ . As for the circumferential samples the lack of catastrophic failure is due to traction.

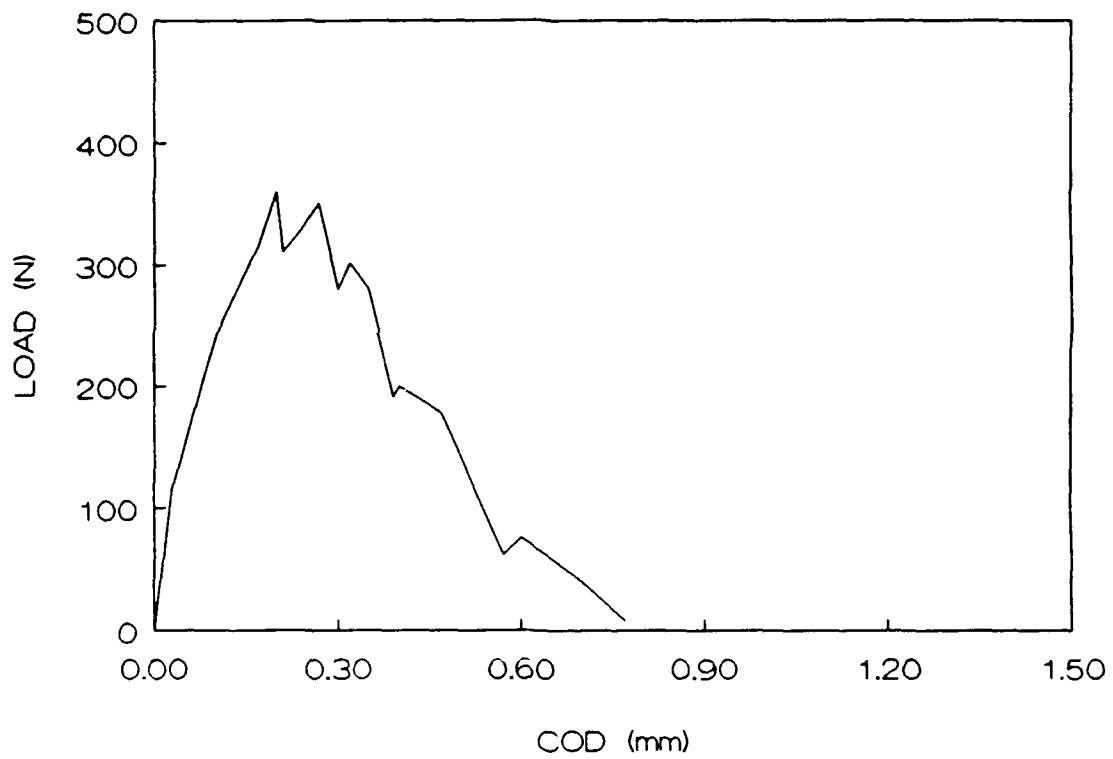
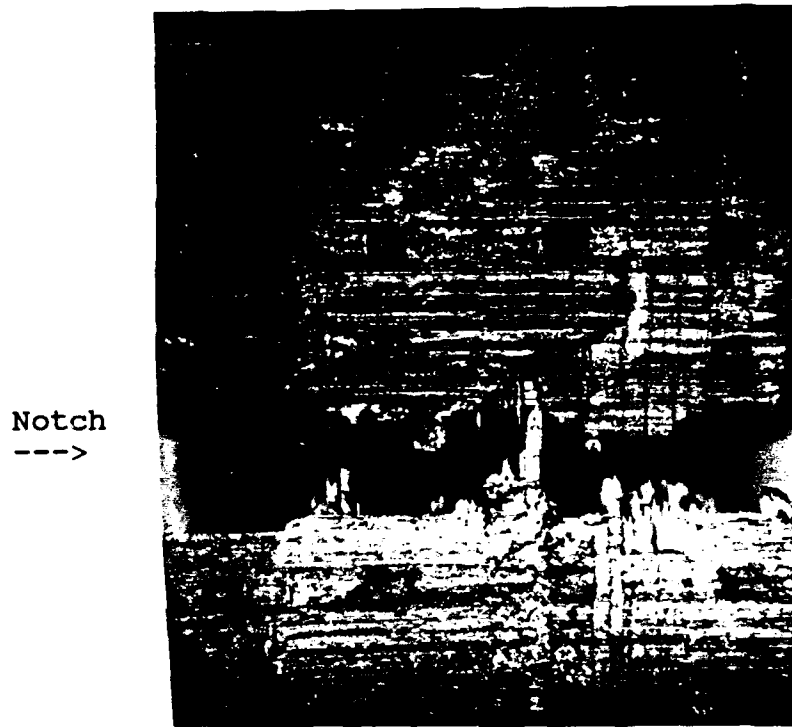


Figure 3.8. Load-displacement curve for an axially-notched sample at an  $a/W$  of 0.2.



3 mm

Figure 3.9. Micrograph of the fracture path of a circumferentially-notched sample at an  $a/W$  of 0.2.

A load-displacement curve for an axially-notched sample at an  $a/W$  of 0.2 is pictured in Figure 3.8. Although the shape does not differ considerably from the other two directions lower loads are achieved for every notch depth and the  $K_{max}$  value remains constant (Table 3.3).

The number of load peaks may be correlated to each fracture process. Figure 3.9 shows a side view of the circumferential sample from Figure 3.6. The three peaks in the curve correspond to the three primary areas of fracture. It is noted that most of the sample had already failed before the maximum load was achieved. Also, the length of the failed axial yarn decreased across the width of the sample due to the increased dominance of the compressive stress. In contrast to the radially-notched samples (Figure 3.10), the degree of individual axial yarn pullout is much higher. The axial yarns of the radial samples failed in "clumps" whereas the circumferentially-notched samples exhibited axial yarn pullout one to two millimeters below and above the mean crack path distinctly separated by radial and circumferential yarns.

The fracture path (Figure 3.10) of the radial sample from Figure 3.7 shows that initiation corresponded to axial yarn failure along a radial yarn above the notch followed by growth along the same yarn. The axial yarns are pulled out around the notch tip and in the area where the crack turns  $90^\circ$  and runs along an axial yarn to a radial yarn below the notch

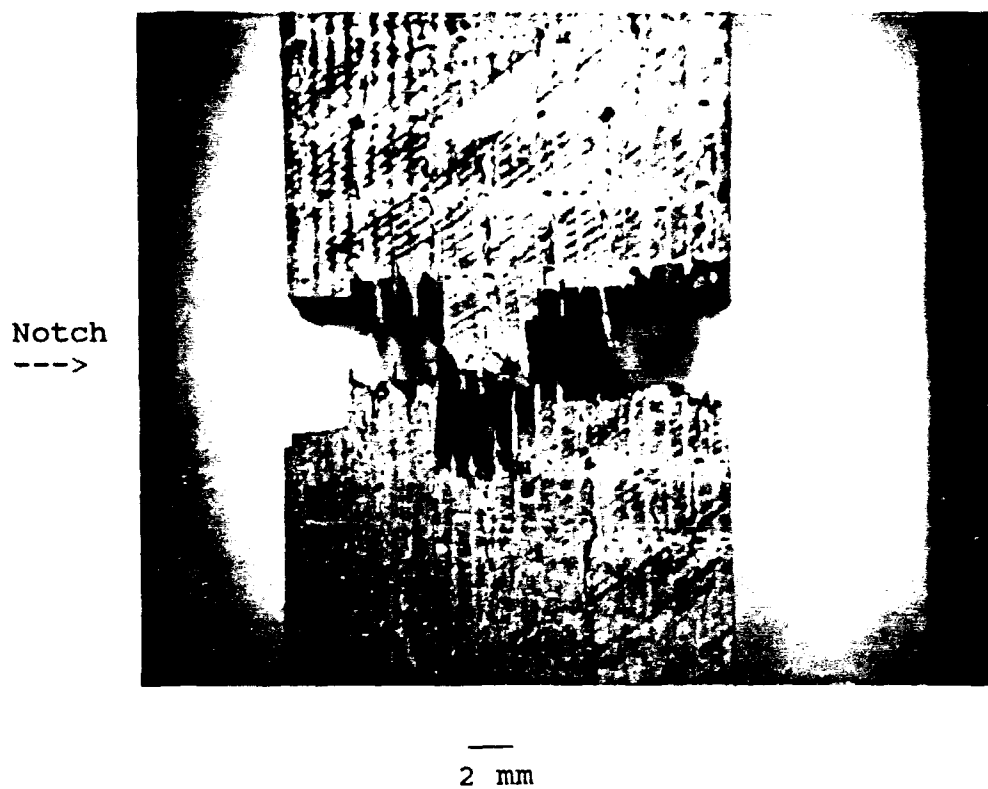


Figure 3.10. Micrograph of the fracture path of a radially-notched sample at an  $a/W$  of 0.2.



plane. The regular fluctuations of the load-displacement curve reflect the constant movement of the crack front between the radial yarns above and below the mean crack path. Propagation occurred along the axial yarn because the shear strength of the axial-circumferential yarn interface is reached before the fiber tensile strength which would precipitate axial yarn failure. At a crack length greater than one-half of the specimen width the surface becomes relatively flat due to the increased dominance of the compressive stress.

In comparison to Figures 3.9 and 3.10, Figure 3.11 illustrates that few of the same fracture processes took place on the axially-notched sample. The crack is seen to begin propagation at the notch tip and then to continue along the axial yarn above the notch. The fracture surface is slanted with propagation occurring from the notch on the back side and along an axial yarn above the notch plane on the front side. The four fractured radial yarns (normal to the crack front) correspond to the load peaks in the load-displacement curve. The crack path of the axially-notched samples was also much more readily observed during testing because of its rectilinear nature.

The difference between fracture mechanisms leading to an increased fracture toughness is readily apparent from the fracture surface (Figures 3.12, 3.13, 3.17). The number of

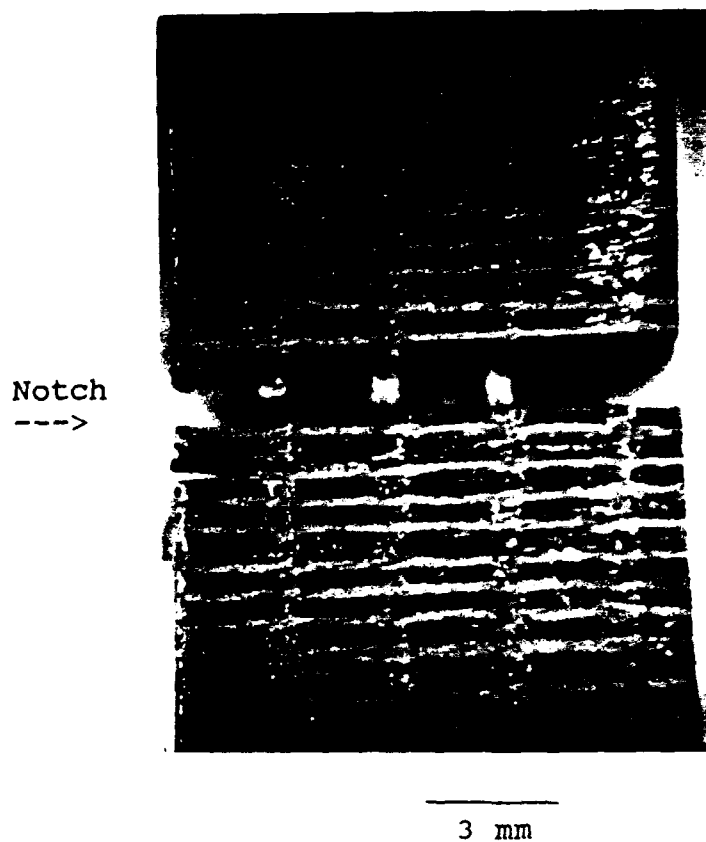
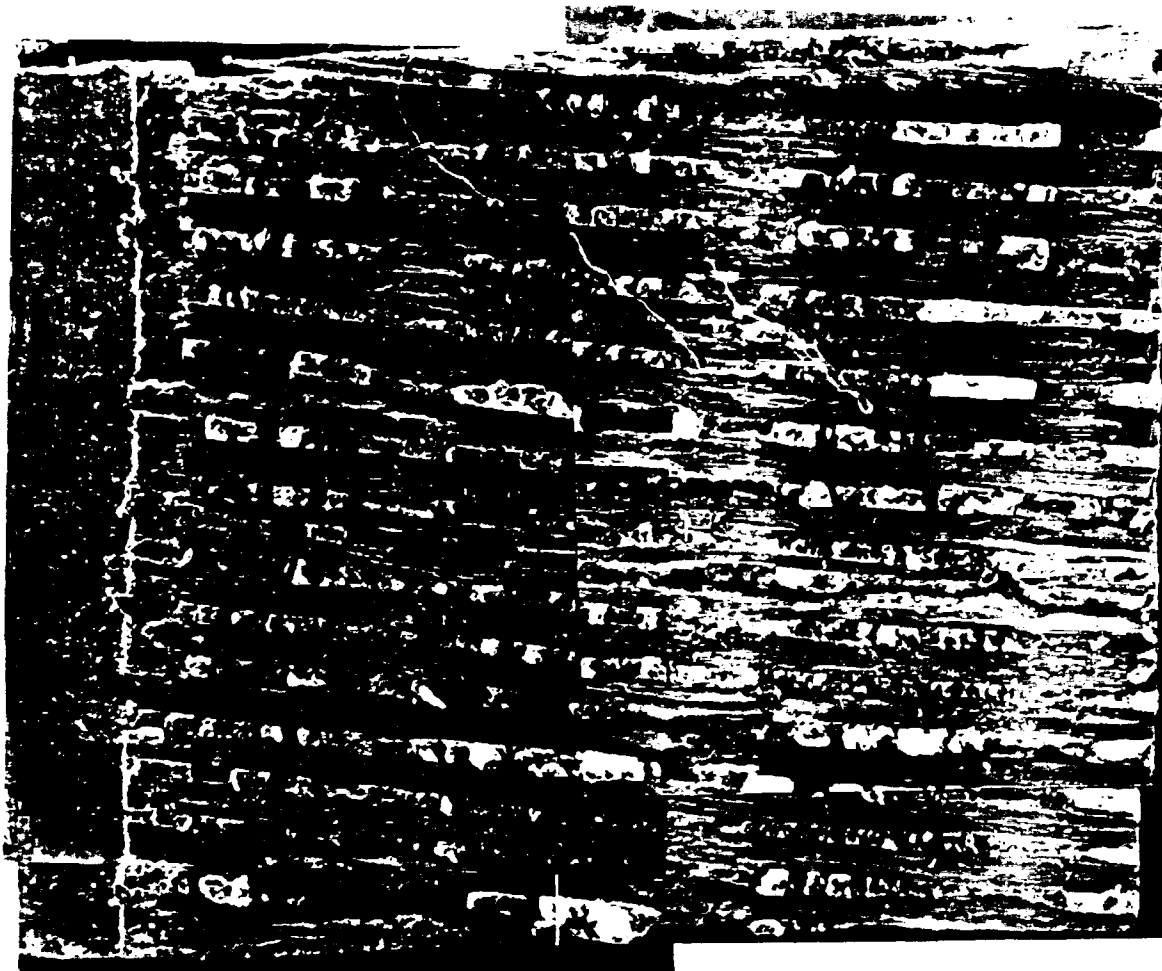


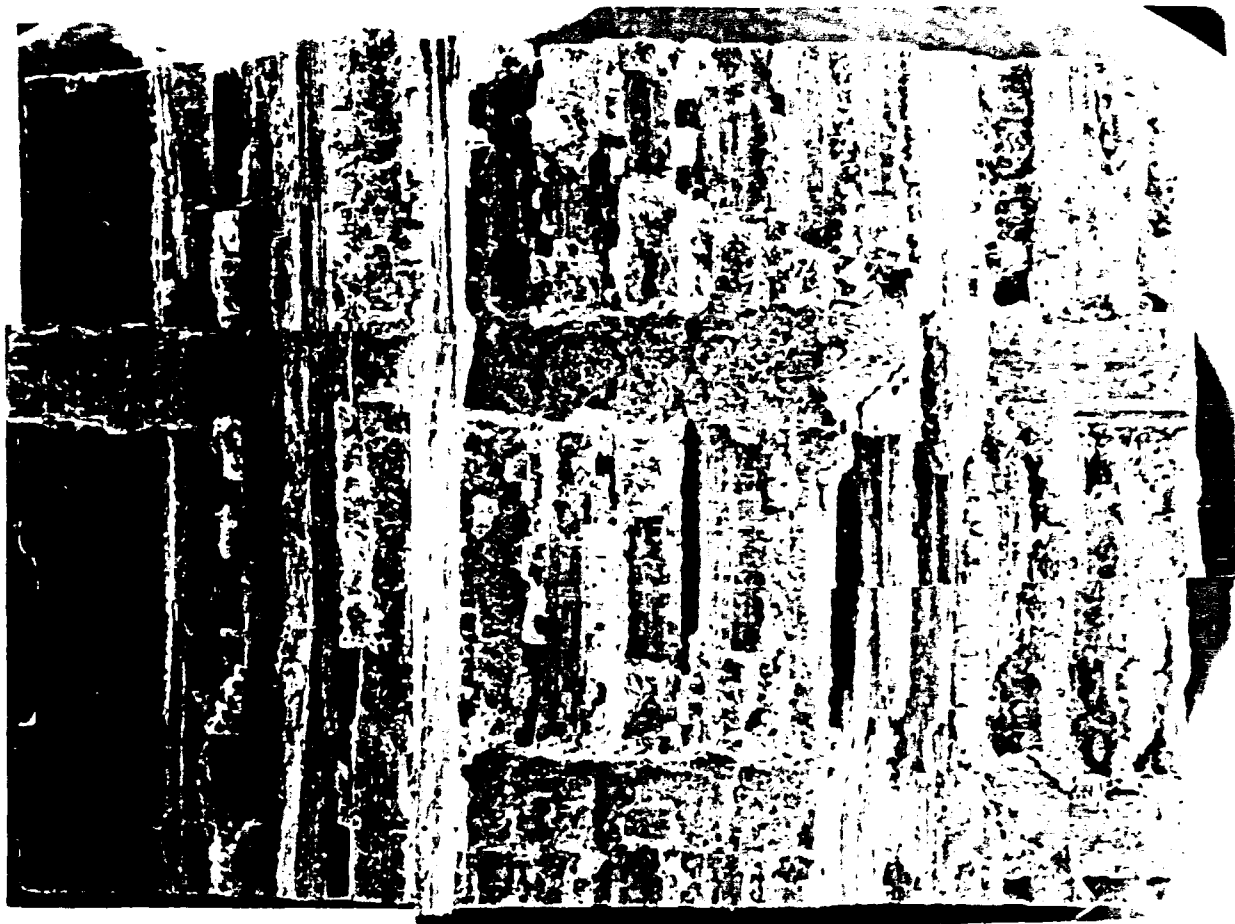
Figure 3.11. Micrograph of the fracture path of an axially-notched sample at an  $a/W$  of 0.2.



Notch  
--->

1 mm

Figure 3.12. Overview of a circumferentially-notched sample at an  $a/W$  of 0.2.



Notch  
--->

1 mm

Figure 3.13. Overview of a radially-notched sample at an  $a/W$  of 0.2.

fracture events occurring appears to be higher than for the other notching directions. Specifically, in the region from the notch front to one-half the specimen width approximately 24 axial yarns experience debonding, fracture and pullout (Figure 3.12). In comparison the radially-notched sample shows only three regions of pullout dominated by a cluster of failure two millimeters from the notch front (Figure 3.13). The fracture surface of a circumferential sample (Figure 3.12) suggests that the alignment of the yarns at an off-angle to the notch front may be partially responsible for the fracture resistance.

Figure 3.14 is an axial yarn bundle from the circumferentially-notched sample of Figure 3.12. The fibers were debonded, fractured and pulled-out. The matrix surrounds the individual fibers in a ribbon-like structure of thin sheets. At higher magnification (Figure 3.15) the ribbons are seen to be graphitic. Graphite increases the strength of the matrix thereby leading to a high fracture resistance. Since identical structures are found on the radially-notched sample (Figure 3.16) the conclusion may be drawn that the higher  $K_{max}$  value (Table 3.3) stems from the yarn density variation and the lower number of large microflaws which facilitated fracture (Figures 3.3 and 3.4) rather than fiber or matrix differences.

The axially-notched samples had the lowest  $K_{max}$  value



Figure 3.14. SEM micrograph of an axial bundle on a circumferentially-notched sample at an  $a/W$  of 0.2.

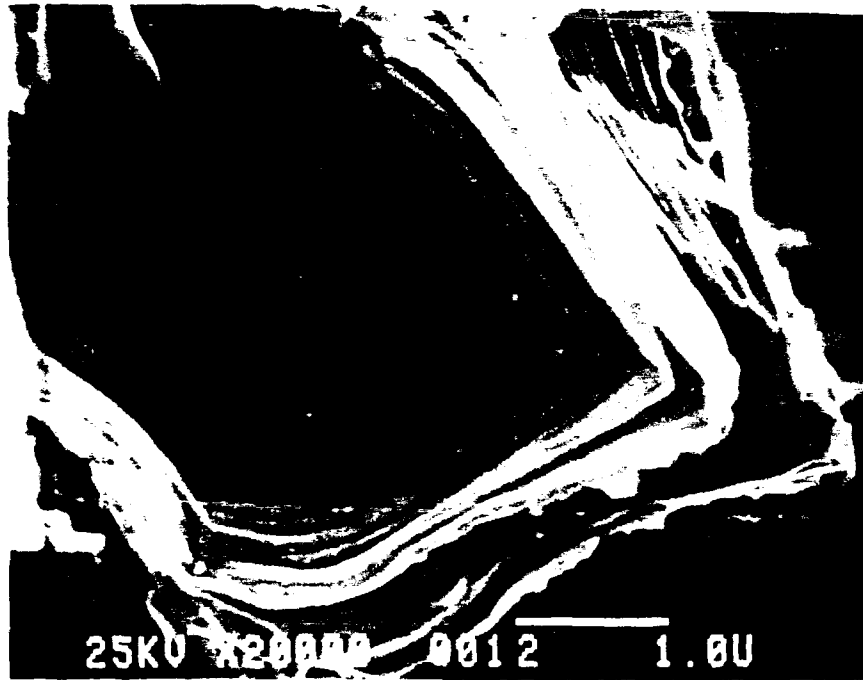


Figure 3.15. Higher magnification SEM photo of axial bundle on circumferentially-notched sample at an  $a/W$  of 0.2 showing layered graphitic structure.



Figure 3.16. SEM micrograph of axial bundle on radially-notched sample at an a/W of 0.2 showing graphitic matrix surrounding fibers.



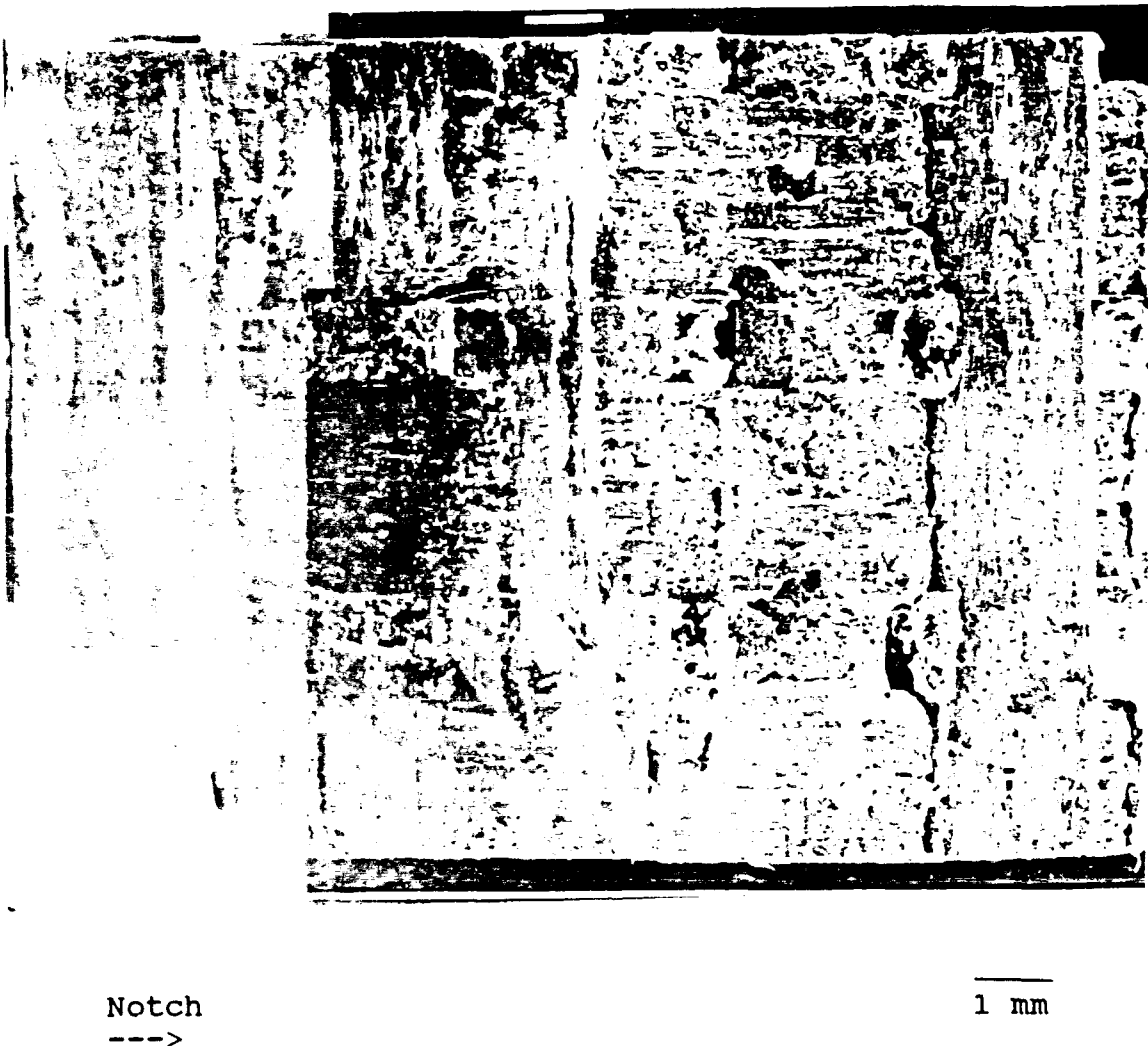


Figure 3.17. Overview of an axially-notched sample fracture surface at an  $a/W$  of 0.5.

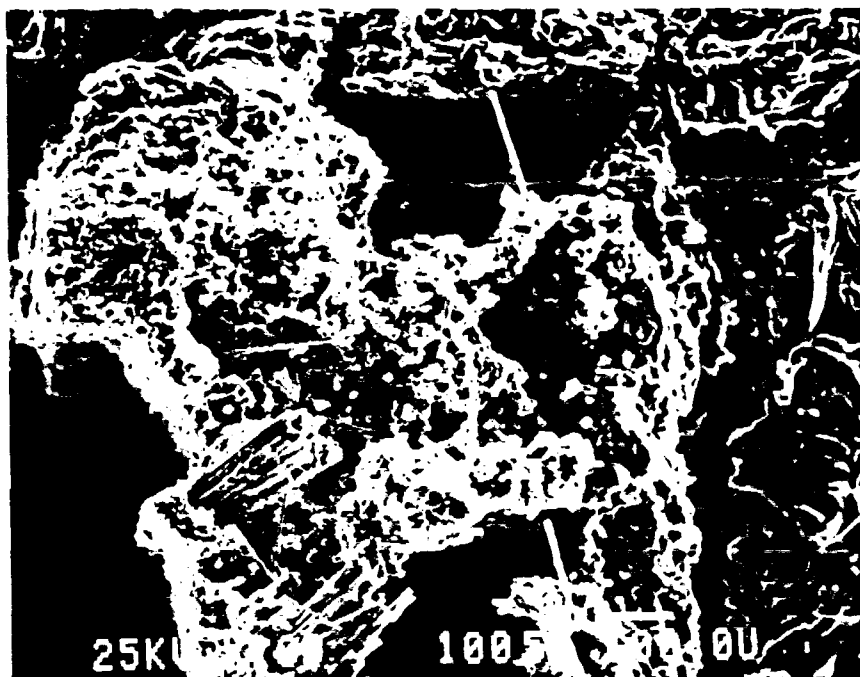


Figure 3.18. SEM micrograph of radial bundle on surface of an axially-notched sample.

which is expected from the lack of fracture mechanisms (Figure 3.17) found on the circumferentially and radially-notched samples. At higher magnification (Figure 3.18) the radial yarns appear to have experienced only a small degree of fiber pullout compared to the circumferential and radial samples (Figures 3.14 and 3.16). Furthermore, because the yarn density perpendicular to the crack tip is lower, the maximum load which corresponds to yarn failure must also be lower. The ability of the material then to provide further crack propagation resistance is a function of the matrix strength. In this respect it may be noted that propagation occurred along the axial-circumferential interface which provided a low energy path due to the presence of microcracks (Figure 3.5). Matrix along the axial (horizontal in photo) and circumferential (vertical) yarns provided planes for crack propagation. The combined effects of low strength and lack of adequate reinforcement perpendicular to the crack growth direction resulted in  $K_{max}$  values one-third to one-fourth those obtained in the other directions (Table 3.3). It should be acknowledged that Figure 3.17 shows a sample at an  $a/W$  of 0.5 and Figures 3.12 and 3.13 samples at an  $a/W$  of 0.2. However, with respect to the axial orientation the fracture surfaces were identical irrespective of notch depth.

#### 3.3.4 Fracture Toughness as a Function of Notch Depth

The average  $K_{max}$  for all orientations is drawn as a function of notch depth in Figure 3.19. For both radial and circumferential samples  $K_{max}$  is a decreasing function of  $a/W$ . In contrast the axially-notched samples were independent of notch depth. The explanation for such behavior lies in consideration of two processes: 1) the simultaneous interaction of the notch with the microflaw field and specimen edge, and 2) the increasing dominance of the compressive stress as the notch depth lengthens. In a homogeneous material, the  $f(a/W)$  correction factor eliminates the edge effects, i.e., the biaxial stress state, on  $K_{max}$ . This is the behavior witnessed for the axially-notched samples and is further substantiated by the fracture surface appearance (Figure 3.17). Fracture processes involving radial yarns and leading to crack growth resistance are limited. The yarns do not protrude further than approximately one millimeter above the notch (Figure 3.10) and do not fail as a coherent unit but as individual fiber clumps. Lastly, the fracture surface shows matrix along the fibers which indicates that the samples failed through the matrix. Therefore, because the fracture involved only the matrix the sample behaved as a continuum and no dependency on notch depth was found.

Contrary to this behavior the fracture processes of the radially and circumferentially-notched samples involved both

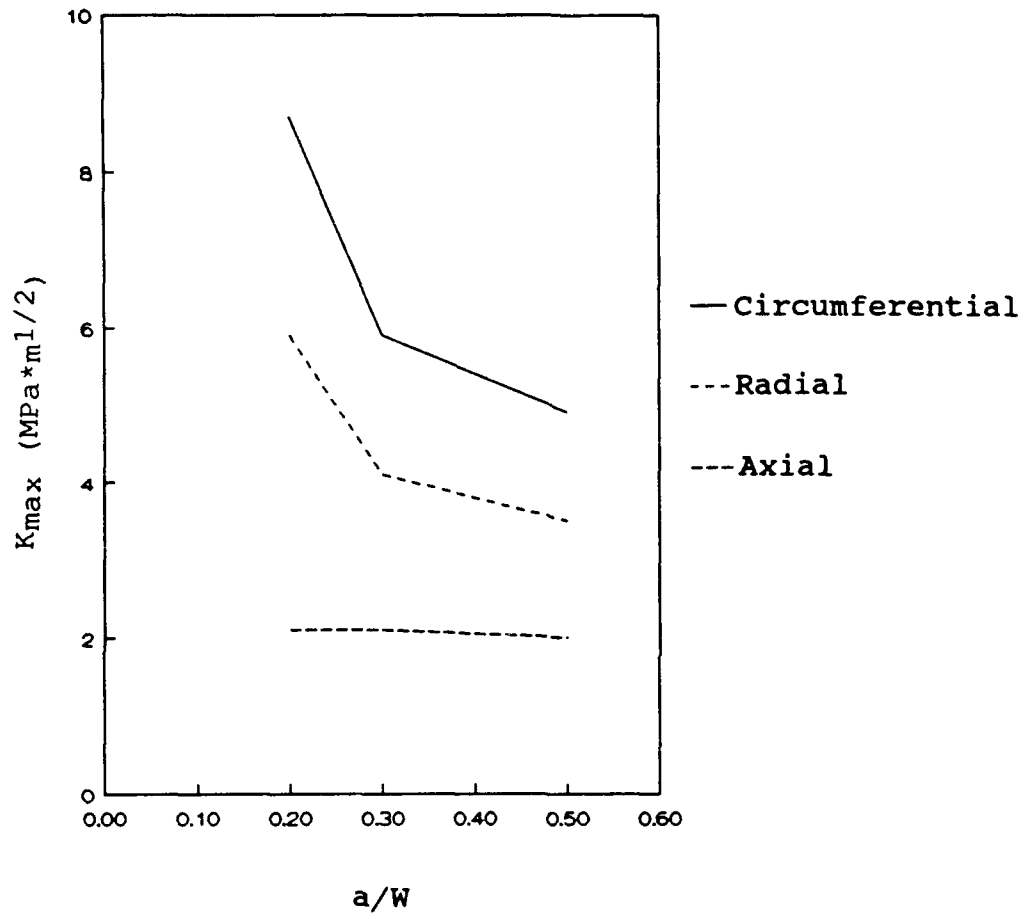


Figure 3.19.  $K_{\max}$  as a function of  $a/W$  for all three notch orientations.

the matrix and yarns. The correction factor does not account for the interactions of the stress and architecture and therefore fracture mechanics are not obeyed.

Secondly, in consideration of the decreasing  $K_{max}$  as a function of  $a/W$ , the behavior reflects the fact that as the compressive stress increases the role of the microdefects and their contribution to the crack front diffusivity decreases. That is, the flaws close in compression and no longer to act to attract the crack into lower energy regions. This reiterates the concept of a microstructural network of microcracks and voids whose influence on the fracture behavior depends on the orientation of the defects with the induced notch direction and depth.

The notch length to width ratio employed for standard fracture toughness determination lies between 0.45 and 0.55. Since  $K_{max}$  was lowest at an  $a/W$  ratio of 0.5, the values obtained may be used as a conservative estimate of the fracture toughness.

The effect of notch location with respect to the radial yarns was also considered for all notch depths. Within the set of twelve samples at an  $a/W$  of 0.2 it was observed that the crack propagated first along an axial yarn perpendicular to the tip and irrespective of whether the notch was through, above, or in between a radial yarn. Although this was still the case at an  $a/W$  of 0.3, as the notch depth increased the

occurrence of axial yarn fracture at the notch tip diminished due to the shift in stress state from tensile to compressive.

### 3.4 CONCLUSIONS

- 1) The composite contains a complex network of microdefects induced during thermal cycling and impregnation. As a result of the anisotropic thermal expansion of the fibers and matrix, compressive and tensile stresses exist. These stresses result in microcracks within the fibers and along the interfaces. Voids are also present as a result of trapped gas bubbles.
- 2) A notch orientation dependence of the  $K_{max}$  parameter is found due to yarn density and microstructural differences. The circumferential direction exhibits the greatest resistance to crack initiation because of the higher cross-sectional area of yarns at the crack front and the smaller flaws. The axial direction is least resistant and contains larger voids and fewer yarns normal to the crack front to provide crack growth resistance.
- 3)  $K_{max}$  for samples notched in the radial and circumferential directions was a decreasing function of notch depth. The dependency is due to the interaction of the architecture consisting of mutually perpendicular yarns and microflaws and sample edge with the stress concentration.
- 4) Axially notched samples did not exhibit any notch length sensitivity and behaved as a homogeneous material in which the

crack is confined to one plane.

5) The  $K_{\max}$  values at an  $a/W$  of 0.5 may be used for design purposes as a conservative estimate of the fracture toughness.



**CHAPTER 4**  
**CRACK DIFFUSION MODEL**

#### 4.1 INTRODUCTION

In the previous two chapters the fracture toughness of 2D and 3D composites has been characterized by  $K_{max}$ . One 2D composite, T300 HT, exhibited a load-specimen dependency which was derived from the presence of microflaws and their interaction with the different stress states. In the case of the 3D composite  $K_{max}$  for the radial and circumferential directions depended on notch depth. Within the three directions the highest  $K_{max}$  was obtained for the circumferential direction which had the highest yarn density at the crack front. The interdependency of the architecture and observed fracture mechanisms was examined in order to clarify the toughening effects of such features.

Although  $K_{max}$  adequately described the resistance to crack initiation, a more thorough description of the fracture process must be derived relating the fracture mechanisms and intrinsic material properties. The crack diffusion model (CDM) is an attempt at just such a theoretical development [53,54]. At this time it has been applied to Kevlar-reinforced polyester [55] and PMMA [56] and 2D C/C composites [57]. Originally computations employing the CDM were performed on a VAX system but it has been rewritten in PASCAL for a PC. The results from the PASCAL program were compared to those obtained from previous work on C/C composites [57]. One of the composites was KKarb C analyzed

in chapter one and the other KKarb A also supplied by Kaiser Aerotech. Lastly, the model was applied to the 3D composite and preliminary results are indicative of the diffuse nature of the fracture process.

#### 4.2 MODEL DERIVATION

The crack diffusion model (CDM) unifies two approaches to fracture studies: fracture mechanics which describe fracture in terms of stress localization, and the weakest-link theory accounting for random processes. A full description of the model may be found in references 53 and 54. The following derivation applies to the four-point and three-point bend geometries.

The CDM assumes the strength field,  $\gamma$ , is randomly fluctuating and characterized by a diffusion coefficient,  $D$ , point wise Weibull distribution,  $F(\gamma)$ , and correlation distance,  $r_0$ . Each parameter can be related to a physical aspect of the crack propagation process. Firstly, the crack advances into low energy sinks or microflaws which do not necessarily lie along the notch plane. Therefore a highly diffusive crack path develops as the crack "seeks" the easiest path for advancement. The crack diffusion coefficient becomes a measure of the deviations from linear crack propagation. Secondly, these weakest links or energy minima of the material suggest the use of the statistics of extremes to describe the

strength field. A Weibull distribution function in terms of  $\gamma$  is written for each advance [58]:

$$(1) \quad F(\gamma) = \begin{cases} 1 - \exp \left( - \frac{\gamma - \gamma_{\min}}{\gamma_0} \right) & \gamma \geq \gamma_{\min} \\ 0 & \gamma < \gamma_{\min} \end{cases}$$

Here  $\gamma_{\min}$  is the minimum energy required for crack initiation,  $\gamma_0$  the inherent surface energy, and  $\alpha$  the shape parameter indicative of the strength field heterogeneity. The values of  $\gamma$  are described by a joint distribution function. At a distance  $r \geq r_0$  the  $\gamma$  values become mutually independent. The  $r_0$  parameter is assigned based upon the material's architecture.

In our study the load at which critical crack propagation occurred,  $Q_c$  was considered the random variable. Its magnitude is a function of the statistical strength field. A distribution function in terms of  $Q_c$  describes the probability that  $Q \leq Q_c$ :

$$(2) \quad F(Q_c) = \exp \left[ - \int_{a_0}^W \exp \left( - \left| \frac{\left( \frac{J(Q_c)}{2} - \gamma_{\min} \right)}{\gamma_0} \right|^\alpha \frac{dx}{r_0} \right) \right]$$

where  $W$  is the sample width,  $a_0$  the notch depth,  $r_0$  the correlation distance,  $J(Q_c)$  the energy release rate and  $\gamma_{\min}$ ,  $\gamma_0$ , and  $\alpha$  Weibull parameters previously described.

The average value of  $\gamma$  is introduced to simplify the calculation of the Weibull parameters:

$$(3) \quad \gamma^* = \gamma_{\min} + \Gamma(1 + \frac{1}{\alpha}) \gamma_0$$

where  $\Gamma(1+1/\alpha)$  is the gamma function. The Weibull function (equation 1) written in terms of the average surface energy becomes:

$$(4) \quad F(\gamma) = 1 - \exp \left[ - \left| \Gamma(1 + \frac{1}{\alpha}) \frac{\gamma - \gamma_{\min}}{(\gamma^* - \gamma_{\min})} \right|^\alpha \right] \quad \begin{matrix} \gamma \geq \gamma_{\min} \\ 0 & \gamma < \gamma_{\min} \end{matrix}$$

Rearrangement and substitution for  $\gamma_0$  in equation two leads to the working equation:

$$(5) \quad F(Q_c) = \exp \left[ - \left| \int_{a_0}^N \exp \left[ - \left| \Gamma(1 + \frac{1}{\alpha}) \frac{(\frac{J(Q_c)}{2} - \gamma_{\min})}{(\gamma^* - \gamma_{\min})} \right|^\alpha \frac{dx}{x_0} \right] \right| \right]$$

By rewriting equation two in terms of  $\gamma_{\min}$ ,  $\gamma^*$  and  $\alpha$  (rather than  $\gamma_{\min}$ ,  $\gamma_0$ , and  $\alpha$ ) two measurable parameters are obtained which may be directly related to material characteristics.

Equation five describes the probability of propagation in terms of three variables. The determination of each parameter requires a three-space analysis. However, equation five may be reduced to a two-variable equation by considering the ratio of the standard deviation of the fracture energy to its average value (coefficient of variation) for a Weibull distribution:

$$(6) \quad \frac{\sigma(\gamma)}{\gamma^*} = (1 - \frac{\gamma_{\min}}{\gamma^*}) \left| \frac{\Gamma(1 + \frac{2}{\alpha})}{\Gamma^2(1 + \frac{1}{\alpha})} - 1 \right|^{1/2}$$

If the energy release rate is considered to have an equivalent ratio then this equation may be rewritten as:

$$(7) \quad \frac{\sigma(\gamma)}{\gamma^*} = \frac{\sigma(J_{IC})}{\langle J_{IC} \rangle} = (1 - \frac{\gamma_{\min}}{\gamma^*}) \left| \frac{\Gamma(1 + \frac{2}{\alpha})}{\Gamma^2(1 + \frac{1}{\alpha})} - 1 \right|^{1/2}$$

The evaluation is carried out for  $\alpha = 1$  and the value of 'q'  $= \gamma_{\min}/\gamma^*$  is substituted into equation five so that it becomes a function of  $\gamma^*$  and  $\alpha$  (Table 4.1).

#### 4.3 DATA ANALYSIS

The most common regression technique, a X-square fit would be applied to a histogram of the critical loads. A minimization of the function  $F(Q_c)$  with respect to  $Q_c$  would give the distribution parameters  $\gamma^*$  and  $\alpha$ . Due to the limited number of samples (five for the KKarb materials and four for the T300 HT composite), the X-square fitting method is not suitable. Therefore, the Kolmogorov-Smirnov measure of agreement was used [59]. For a sample set of size,  $N$ , an experimental step function,  $F_{\text{exp}}(Q_c)$  is drawn with  $N$  discrete jumps of  $1/N$  at each critical load. The distribution function is compared to the experimental function at each  $Q_c$  through the variable,  $d$ :

Table 4.1  
Coefficient of Variation and 'q' Values  
Used in CDM Calculations

	KKarb A	KKarb C	T300 HT	3D
$\frac{\sigma(J_c)}{\langle J_c \rangle}$	0.06	0.25	0.21	0.21
q	0.90	0.65	0.79	0.79

$$(8) \quad d = \max_i \left| F(Q_c) - F_{\text{exp}}(Q_c) \right|$$

$$d = \max_{i, \dots, N} \left| F(Q_{ci}) - \frac{i}{N} \right|, \left| F(Q_{ci}) - \frac{(i-1)}{N} \right|$$

The critical loads must be ordered such that  $Q_{i-1} \leq Q_i$ .

The value of  $\gamma^*$  is first approximated in order to limit the search time for the minimum in  $d$ . For crack initiation the energy release rate,  $J_c$  must be greater than or equal to twice the inherent surface energy  $\gamma_{\min}$ . Then  $\gamma^*$  is related to  $\gamma_{\min}$  through the  $q$  parameter:

$$J_c \geq 2\gamma_{\min} \geq 2(q\gamma^*)$$

The upper limits for  $\gamma^*$  are presented in Table 4.2. The optimum values of  $\gamma^*$ ,  $\gamma_{\min}$ , and  $\alpha$  are found by minimizing  $d$ .

#### 4.4 RESULTS AND DISCUSSION

The model had been previously applied to two 2D composites using a VAX to perform the calculations. The PASCAL program was written in order to remove the dependence of the user on a VAX system.

##### 4.4.1 2D Results

The maximum loads and energy release rates for the three composites are presented in Table 4.3. The critical loads for the T300 HT composite are seen to vary over a greater range than for the KKarb materials. It is suggested that the load



Table 4.2  
Upper Limits of  $\gamma^*$   
for 2D Composites

Composite	$\gamma^*$ (J/m <sup>2</sup> )
KKarb A	851
KKarb C	2325
T300 HT	215

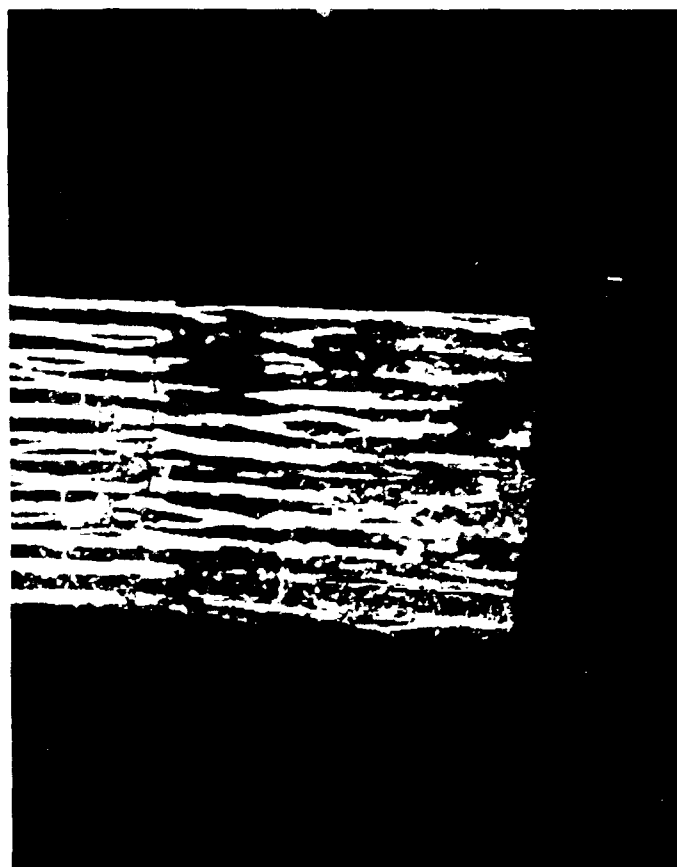
Table 4.3  
Critical Loads and Energy  
Release Rates for 2D Composites

Composite	$Q_c$ (N)	$J_c$ (J/m <sup>2</sup> )
KKarb A	1423	1533
	1453	1598
	1456	1605
	1468	1631
	1497	1696
KKarb C	710	2993
	725	3121
	750	3337
	760	3423
	770	3509
T300 HT	876	233
	1068	348
	1073	351
	1201	441

variability resulted from the microflaw type and distribution. The primary microdefects in both KKarb composites were microcracks which are present to a much smaller extent in the T300 HT composite. The microcrack populations of the KKarb A and C composites were 3875 and 2165 per  $\text{cm}^2$  respectively whereas the T300 HT was only 375 per  $\text{cm}^2$ . Microvoids along the plies and between the yarn bundles compose the microdefect field of the T300 HT material. The sample which had the lowest maximum load (Figure 4.1) had a smaller region of dominant tensile stress (see chapter on 2D composites). Additionally the yarns fractured in Region F of the sample which had the highest maximum load (Figure 4.2) were 3-4 millimeters above the mean crack path whereas yarn fracture in the former sample was in the notch plane. The interaction of the compressive stress with the microvoids is also significantly less in the lower  $P_{\max}$  sample because the sample bulges to a lesser extent than in the high  $P_{\max}$  sample (Figure 4.3).

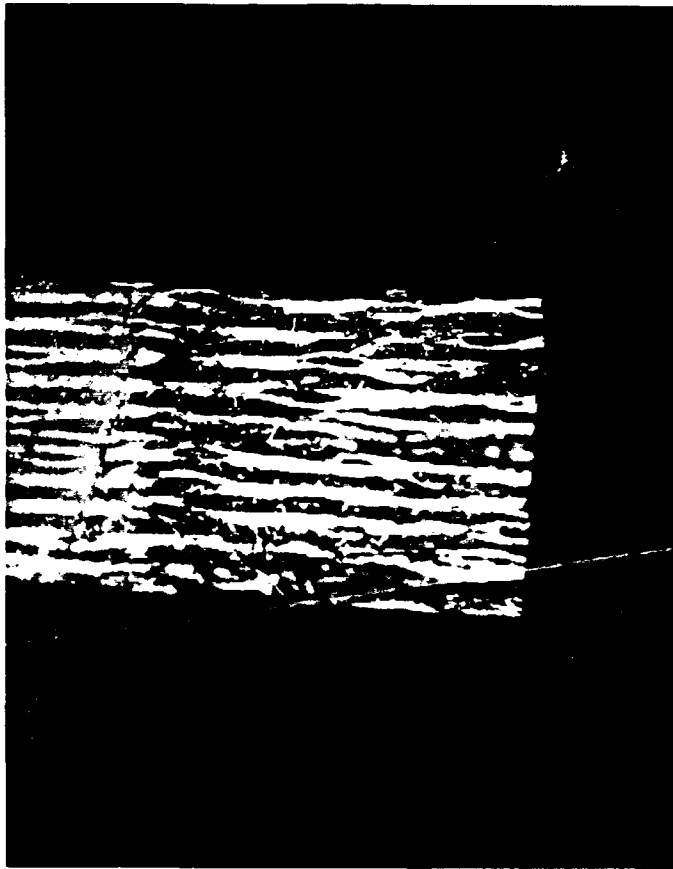
The correlation distance for all three materials was chosen to be 0.1 mm as this corresponds to the distance between plies. Obviously a more rigid approach is necessary which will correlate distinct fracture events with the dimensions separating their occurrence.

The values obtained using the PASCAL program gave the same results as those obtained from the VAX (Table 4.4). The



2 mm

Figure 4.1. Overview of T300 HT composite with  $P_{\max} = 876\text{N}$ .



2 mm

Figure 4.2. Overview of T300 HT composite with  $P_{\max} = 1201\text{N}$ .



2 mm

Figure 4.3. End views of T300 HT composite. Sample on the right had a  $P_{max} = 876N$  and that on the left a  $P_{max}$  of 1201N.

Table 4.4  
VAX and PASCAL Program Results  
for KKarb A and C Composites

<u>Material</u>	<u>VAX</u>		<u>PASCAL</u>	
	$\gamma^*$ (J/m <sup>2</sup> )	$\alpha$	$\gamma^*$ (J/m <sup>2</sup> )	$\alpha$
KKarb A	830	5.4	830	5.0
KFarb C	1500	4.0	1530	4.0

Table 4.5  
CDM Parameters for 2D Composites

Composite	$\gamma^*$ (J/m <sup>2</sup> )	$\gamma_{min}$ (J/m <sup>2</sup> )	$\alpha$
KKarb A	830	775	5.4
KKarb C	1530	995	4.0
T300 HT	160	125	1.4



parameters obtained for the T300 HT composite as well as those for the two KKarb materials are summarized in Table 4.5. The results provide a means through which the role of microflaws on fracture behavior may be mathematically assessed. Namely, the effect of the microcracks is inconsequential in the T300 HT composite compared to the voids. The voids are lower energy sinks than the microcracks because of their size. Hence, the average surface energy,  $\gamma^*$ , is lower. The high microcrack density of the KKarb composites causes the microcracks to act as a continuous line along which the crack progresses as soon as yarn fracture takes place. That is, the crack encounters another microcrack relatively close to the point of yarn fracture. The microcracks act as discriminating microstructural features in that the lower  $\gamma^*$  is obtained for the KKarb A composite which has shorter microcracks [40].

It is valuable to note that the  $K_{max}$  value obtained for the T300 HT composite was 3-4 times higher than that of the KKarb C composite. However, the average surface energy of the former is one-eighth that of the latter. This observation indicates that although the  $\gamma^*$  value reflects the size of the microflaw, alone it incompletely accounts for the diffusivity leading to the higher fracture toughness. A lower value of  $\alpha$  reflects the presence of the voids in the T300 HT composite leading to a higher  $K_{max}$  and a more diffuse fracture path (Figures 2.18). The higher values of  $\alpha$  for the KKarb

materials indicate that the microcracks, while effective toughening agents, guide the crack front along a straighter path than found in the T300 HT composite.

#### 4.4.2 3D Composite

The model was also applied to the 3D C/C composite for the twelve specimens tested in the radial direction. The average critical load for the twelve samples was  $877 \pm 94$  N. The CDM parameters  $\gamma^*$ ,  $\gamma_{\min}$ , and  $\alpha$  were  $420 \text{ J/m}^2$ ,  $328 \text{ J/m}^2$  and 1.0, respectively for a minimum  $d$  of 0.214. The low Weibull modulus is an indication of the variance in the material strength field. To illustrate the effect that the wide distribution of loads has on the shape parameter and average fracture energy the program was run for 5, 7, 9, and 12 point data sets as well as the data set corresponding to the standard deviation (Figures 4.4-4.8). The  $\gamma^*$  did not vary across the complete sampling but the shape parameter decreased from 2.6 to 1.0 as the number of data points increased. Interestingly the standard deviation sample set yielded a Weibull modulus of 1.0 indicating that these loads represent the material behavior in the same way as all twelve critical loads.

It would be helpful to have another 3D material as a database in order to compare microstructural effects and ultimately  $\gamma^*$ ,  $\gamma_{\min}$ , and  $\alpha$ .

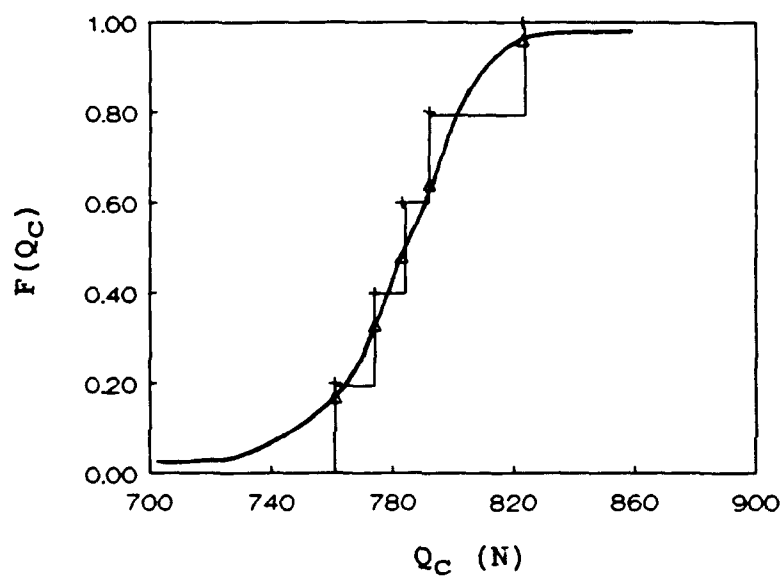


Figure 4.4. Distribution function versus critical load for five critical loads for the 3D composite tested in the radial direction at an  $a/W$  of 0.2.

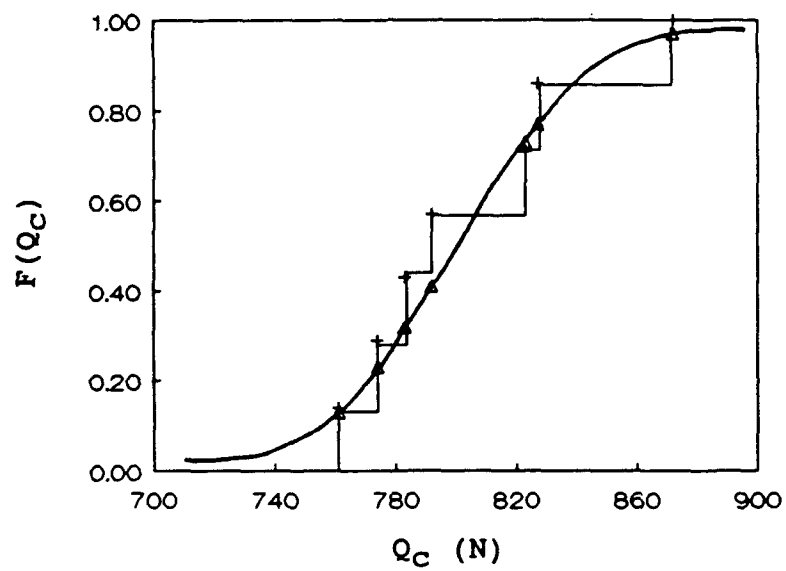


Figure 4.5. Distribution function versus critical load for seven critical loads for the 3D composite tested in the radial direction at an  $a/W$  of 0.2.

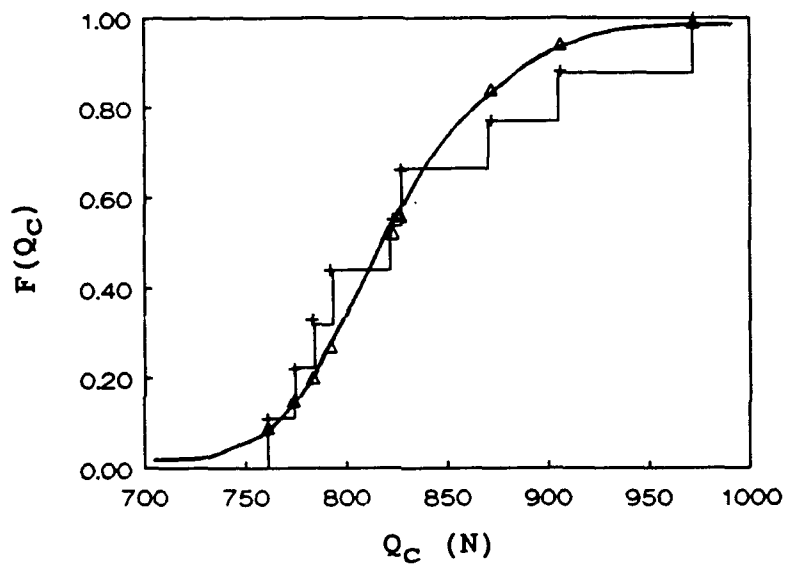


Figure 4.6. Distribution function versus critical load for nine critical loads for the 3D composite tested in the radial direction at an  $a/W$  of 0.2.

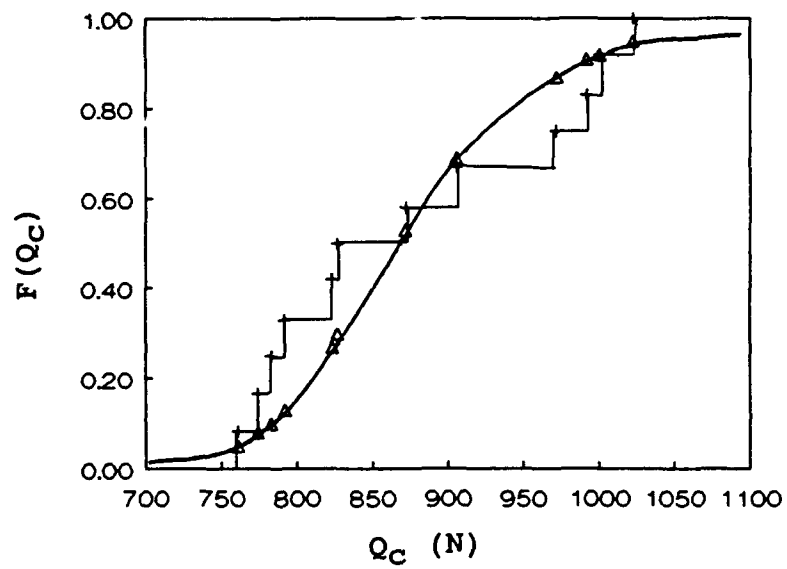


Figure 4.7. Distribution function versus critical load for all twelve critical loads for the 3D composite tested in the radial direction at an  $a/W$  of 0.2.

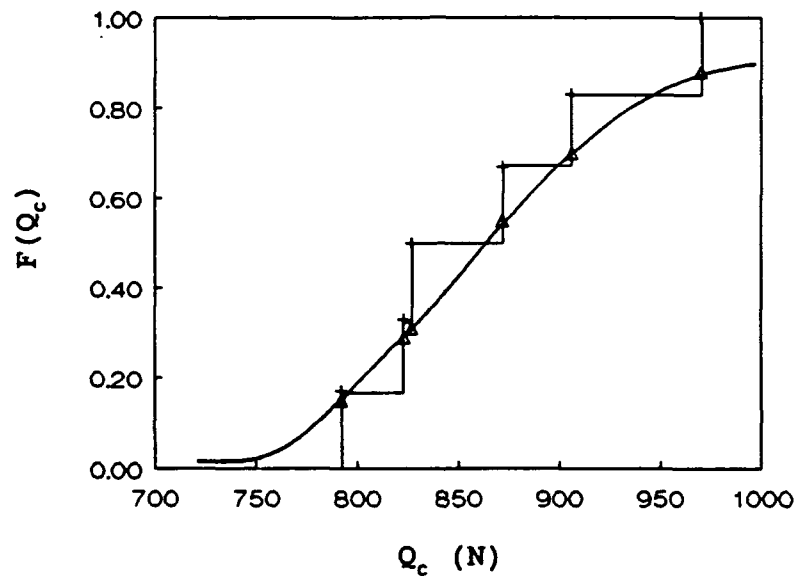


Figure 4.8. Distribution function versus critical load for the six critical loads corresponding to the standard deviation sample set for the 3D composite tested in the radial direction at an  $a/W$  of 0.2.

#### 4.5 CONCLUSIONS

1) The crack diffusion model may be used to determine the average and minimum surface energies which are related to the microstructure of the material. Additionally, the  $\alpha$  value describes the heterogeneity associated with the strength field.

2) The type, number, and distribution of flaws in the 2D composites distinguished them from one another in the analysis using the CDM. A higher density of larger microdefects, i.e., voids, resulted in a lower  $\gamma^*$ . Secondly, the load variability of the T300 HT composite was a reflection of the type of flaw since this composite had more voids than either of the KKarb materials. The interaction of voids perpendicular to the crack front and the imposed stress state determines the crack path direction and ultimate fracture toughness.

3) Application of the CDM to the 3D composite using the PASCAL program yielded a moderate average surface energy in comparison to the 2D materials and a low Weibull modulus.



## CONCLUSIONS

The fracture behavior of carbon/carbon composites has been characterized using  $K_{\max}$  as a parameter to describe the resistance to crack initiation. The results have been related to the material microstructure and fracture mechanisms.

In the first part of the work two 2D composites were evaluated. The dependence of  $K_{\max}$  on testing geometry and thickness was examined. The first composite, KKarb C was composed of rayon fibers woven into a plain weave configuration in a phenolic resin matrix. The second, T300 HT was made of PAN fibers in an 8-harness weave with a pitch matrix. The microdefect field differed in that the KKarb C composite had primarily microcracks extending between the plies whereas the T300 HT material had voids along the plies. The KKarb C composite exhibited no dependence on either thickness or geometry and had an average  $K_{\max}$  of  $5.4 \text{ MPa}\cdot\text{m}^{1/2}$ . The fracture surfaces of all configurations were similar and showed a variety of mechanisms including yarn fracture, and fiber debonding and pullout. In contrast the T300 HT composite had a much higher  $K_{\max}$  and was also dependent on testing geometry. The four-point bend and compact-tension samples had an average  $K_{\max}$  of  $16 \text{ MPa}\cdot\text{m}^{1/2}$  but the value for the SEN samples was  $26 \text{ MPa}\cdot\text{m}^{1/2}$ . Two reasons are offered for these results. First, the T300 HT microstructure consisted of voids perpendicular to the notch acting as low energy sinks into

which the crack preferentially propagated. Hence,  $K_{max}$  increases because the crack is deflected from its original path and must pass through a yarn before advancing further. Secondly, the SEN sample fracture surfaces showed yarn fracture to a greater extent than the 4PB and CT samples. The larger active zone required more energy to develop and therefore the resistance to crack initiation was greater.

In the second part of this work the  $K_{max}$  for a 3D composite was determined as a function of notch orientation and depth. Samples notched in the circumferential direction showed the highest  $K_{max}$  value across all notch depths. The higher yarn density at the crack front provided a greater resistance to crack initiation than in the radial and axial direction. Additionally the crack front encountered yarns at an off-angle to the notch which may have contributed to the fracture toughness. Both the radial and circumferential directions displayed a decreasing dependence of  $K_{max}$  on notch depth. In the axial direction however, the value remained constant and was lower than that obtained for the other two directions. The fracture surface was featureless and showed none of the mechanisms characteristic of the radial and circumferential samples. The fracture toughness obtained at an  $a/W$  of 0.5 for all notching directions may be used as a conservative design parameter since it yields the lowest  $K_{max}$  value.

The crack diffusion model was introduced and applied to three composites in this study. The previous calculations have used a VAX system but in order to make the model more "user-friendly" a PASCAL program for the PC was written. For the 2D composites it was found that the more heterogeneous the microstructure the lower the average surface energy. Moreover, the same material had a lower Weibull modulus indicative of the variability of the strength field. The application of the CDM to the 12 3D samples notched in the radial direction yielded a moderate surface energy in comparison to the 2D composites. Further examination of the microstructure and the assignation of a correlation distance are necessary before additional conclusions may be drawn.

## REFERENCES

- 1). K. Chawla, Composites, Springer-Verlag, New York, (1987).
- 2). D. L. Schmidt, "Carbon/Carbon Composites," SAMPE J., 8(3), 9 (1972).
- 3). L.M. Sheppard, "Challenges Facing the Carbon Industry," ACS Bulletin, 67(12), 1897, (1988).
- 4). D.J. Johnson, In Introduction to Carbon Science (Edited by H. Marsh), pp. 197-228, Butterworths, London, 1989.
- 5). D.J. Johnson, In Introduction to Carbon Science (Edited by H. Marsh), pp. 200-201, Butterworths, London, 1989.
- 6). K.S. Singer, "The Mesophase and High Modulus Carbon Fibres from Pitch," Carbon, 16, 409, (1978).
- 7). D.J. Johnson, In Introduction to Carbon Science (Edited by H. Marsh), p. 226, Butterworths, London, 1989.
- 8). D. Hull, An Introduction to Composite Materials, Cambridge University Press, Cambridge, (1981), p.13.
- 9). J.B. Barr, S. Chwastiak, R. Didchenko, I.C. Lewis, R.T. Lewis, L.S. Singer, "High Modulus Carbon Fibers from Pitch Precursor," Appl. Poly. Symp., 29, 161, (1976).
- 10). H.M. Stoller, B.L. Butler, J.D. Theis, M.L. Lieberman, In Composites: State of the Art, (Edited by J. W. Weeton, E. Scala), pp. 69-136, Proceedings of ASME Fall Meeting, Dearborn, 1971.
- 11). J.D. Buckley, "Carbon-Carbon, An Overview," ACS Bulletin, 67(2), 364, (1988).
- 12). D.F. Adams, "Transverse Tensile and Longitudinal Shear Behavior of Unidirection Carbon/Carbon Composites," Mat. Sci. Eng., 17, 139, (1975).
- 13). J.L. Perry, D.F. Adams, "An Experimental Study of Carbon-Carbon Composite Materials," J. Mat. Sci., 9, 1764, (1974).
- 14). D.F. Adams, J. C, "Longitudinal Tensile Behavior of Unidirectional C/C Composites," J. Comp. Matls., 8, 320, (1974).
- 15). L.E. McAllister, W.L. Lachman In Handbook of Composites, Vol. 4-Fabrication of Composites (Edited by A. Kelly, S.T. Milieko), Elsevier, Amsterdam, (1981), pp. 109-175.

- 16). C.T. Robinson, "Damage Mechanisms and Failure of 3-D Carbon-Carbon Composites," SRI Report, May 1981.
- 17). F.I. Clayton, D.A. Eitman, "Material Property Characterization Results for 7-Inch Carbon-Carbon Bilet Program," AFML Report, January 1980.
- 18). A.J. Klein, "Carbon/Carbon Composites," Adv. Matl. & Prog., 11, 64, 1986.
- 19). S-M. Oh, J-Y. Lee, "Fracture Behavior of Two-Dimensional Carbon/Carbon Composites, " Carbon, 27(3), 423, 1989.
- 20). W. Kowbel, C.H. Shan, "The Mechanism of Fiber-Matrix Interactions in Carbon-Carbon Composites, " Carbon, 28(2/3), 287, 1990.
- 21). L.M. Manocha, O.P. Bahl, "Influence of Carbon Fiber Type and Weave Pattern on the Development of 2D Carbon-Carbon Composites," Carbon, 26(1), 13, (1988).
- 22). S.N. Chatterjee, In Thermomechanical Behavior of High-Temperature Composites, (Edited by J. Jortner), ASME AD-04, pp. 51-62, American Society of Mechanical Engineers, (1982).
- 23). J. Jortner, In Thermomechanical Behavior of High-Temperature Composites, (Edited by J. Jortner), ASME AD-04, pp. 19-34, American Society of Mechanical Engineers, (1982).
- 24). G. Sines, B. Cohen, In Thermomechanical Behavior of High-Temperature Composites, (Edited by J. Jortner), ASME AD-04, pp. 63-75, American Society of Mechanical Engineers, (1982).
- 25). J. Jortner, "Macroporosity and Interface Cracking in Multi-Directional Carbon-Carbons," Carbon, 24(5), 603, 1986.
- 26). D.F. Adams, "Micro-Analysis of the Behavior of a Three-Dimensionally-Reinforced Carbon-Carbon Composite Material," Matls. Sci. and Eng., 23, 55, (1976).
- 27). J.L. Perry, D.F. Adams, "Mechanical Tests of a Three-Dimensionally Reinforced Carbon-Carbon Composite Material," Carbon, 14, 61, 1976.
- 28). L.H. Peebles, R.A. Meyer, J. Jortner, In Interfaces in Polymer, Ceramic, and Metal Matrix Composites, (Edited by H. Ishida), pp. 1-16, Elsevier, New York, (1988).

- 29). A.A. Griffith, "The phenomena of rupture and flow in solids," Phil. Trans. Roy. Soc. London, 221A, 163, (1920).
- 30). G.R. Irwin, "Analysis of Stresses and Strains Near the End of a Crack Transversing a Plate," ASME, J. of Appl. Mech, (1957).
- 31). G.E. Dieter, Mechanical Metallurgy, pp. 253-260, McGraw-Hill Book Co., New York, (1976).
- 32). ASTM Standard E399-81, Standard Test Method for Plane Strain Fracture Toughness of Metallic Materials, 1981.
- 33). M.R. Piggott, "Theoretical estimation of fracture toughness of fibrous composites," J. Mat. Sci., 5, 669, (1970).
- 34). G.Sih, E. Chen, "Fracture Analysis of Unidirectional Composites," J. Comp. Matls., 7(4), 230, (1973).
- 35). J.K. Wells, P.W.R. Beaumont, "Debonding and pullout processes in fibrous composites," J. Mat. Sci., 20, 1275, (1985).
- 36). M.F. Kanninen, E.F. Rybicki, H.F. Brinson, "A critical look at current applications of fracture mechanics to the failure of fibre-reinforced composites," Composites, 1, 17, (1977).
- 37). T.R. Guess, W.R. Hoover, "Fracture Toughness of Carbon-Carbon Composites," J. Comp. Matls., 7, 2, (1973).
- 38). H.C. Kim, K.J. Yon, R. Pickering, P.J. Sherwood, "Fracture toughness of 2-D carbon fibre reinforced composite materials," J. Mat. Sci., 20, 3967, (1985).
- 39). H. Aglan, A. Moet, In Design and Manufacturing of Advanced Composites, Proc. of 5th Annual ASM/ESD Advanced Composites Conference, Dearborn, 1989.
- 40). H. Aglan, A. Moet, B. Kunin, A. Chudnovsky, "A Probabilistic Analysis of the Strength Field Parameters of Carbon-Carbon Composites," ONR Report #N00014-86-K-0285, July 1989.
- 41). M. Jenkins, J. Mikami, T. Chang, A. Okura, "Effect of Fibre Content on the Fracture Resistance of Carbon Fibre/Carbon Matrix Composites," SAMPE J., 24(3), 32, (1988).

- 42). G. Griesheim, Masters Thesis, Southern Illinois University at Carbondale, (1989).
- 43). J. Zimmer, personal communication.
- 44). H. Tada, P. Paris, G.R. Irwin, The Stress Analysis of Cracks Handbook, Del Research Corporation, Hellertown, (1973).
- 45). J.C. Halpin, K.L. Jerina, T.A. Johnson, ASTM STP 521, 5-11, (1973).
- 46). S.S. Wang, J.F. Mandell, F.J. McGarry, ASTM STP 593, 36-42, (1975).
- 47). K.J. Konish, T.A. Cruse, ASTM STP 580, 490-497, (1975).
- 48). J. Jortner, "Effects of Crimp Angle on Tensile and Compressive Strengths of KKarb 1200 Carbon-Carbon Composites," JANNAF Rocket Nozzle Tech. Subcommittee Meeting, NASA Marshall Space Flight Center, (1988).
- 49). P. Pollock, "Tensile Failure in 2-D Carbon-Carbon Composites," Carbon, 28(5), 717, 1990.
- 50). C.T. Robinson, P.H. Francis, ASTM STP 723, 85-100, (1981).
- 51). D. Phillips, J. Comp. Matls., 8(4), 156, (1974).
- 52). R.T. Potter, "On the mechanism of tensile fracture in notched fibre reinforced plastics," Proc. Roy. Soc. London, 361A, 325, (1978).
- 53). A. Chudnovsky, B. Kunin, J Appl. Phys., 62, 10, (1987).
- 54). A. Chudnovsky, B. Kunin, In Computational Mechanics of Probabilistic and Reliability Analysis, (Edited by T. Belytschko, W.K. Liu), p. 396, Elsevier Press International, CITY?, (1989).
- 55). M.A. Mull, A. Chudnovsky, A. Moet, Phil. Mag., 56, 419, (1987).
- 56). R. Dearth, Masters Thesis, Case Western Reserve University, 1989.
- 57). A. Moet, I. Mostafa, B. Kunin, A. Chudnovsky, "Probabilistic Fracture Mechanics of 2D Composites," in press.

58). Weibull, W., "A statistical theory of the strength of materials," 151:1-45, 153:1-53, Ing. Ventenskags Acad handling, Stockholm, 1936.

59). W.H. Press, B.P. Flannery, S.A. Teukolsky, W.T. Vetterling, Numerical Recipes, Cambridge University Press, Cambridge, (1987).



```
PROGRAM EVAL(INPUT,OUTPUT);
```

```
{THIS PROGRAM WAS WRITTEN TO EVALUATE THE VALUE OF THE KOLMOGOROV-SMIRNOV  
TEST FOR TWO-DIMENSIONAL CARBON/CARBON COMPOSITES IN FOUR-POINT BENDING  
CONFIGURATION}
```

```
USES  
CRT;
```

```
TYPE  
QC = ARRAY[1..12] OF REAL;  
INIT = ARRAY[1..100] OF REAL;  
GAMINIT = ARRAY[1..100] OF REAL;  
ALPINIT = ARRAY[1..100] OF REAL;  
DATAREC = RECORD  
    MAX : INIT;  
    DGAMMA : GAMINIT;  
    DALPHA : ALPINIT;  
END;
```

```
DATAFILE = FILE OF DATAREC;
```

```
VAR  
CMAX, GFOUND, AFOUND : REAL;  
KEEPDATA : DATAFILE;  
GIMMEREK : DATAREC;
```

```
FUNCTION GAM(ALPHADUM:REAL):REAL;
```

```
{COMPUTES THE GAMMA FUNCTION VALUE IN THE INTEGRAL}
```

```
CONST  
FPF = 5.5;  
ONE = 1.0;  
HALF = 0.5;  
STP=2.5066;
```

```
VAR  
COF:ARRAY[1..6] OF REAL;  
GAMMALN,X,SER,TMP:DOUBLE;  
I:INTEGER;  
ALPHANEW:REAL;
```

```
BEGIN  
COF[1]:=76.18009173;  
COF[2]:=-86.50532033;  
COF[3]:=24.01409822;  
COF[4]:=-1.231739516;  
COF[5]:=0.120858003E-2;  
COF[6]:=-0.536382E-5;  
ALPHANEW:= 1 + 2/ALPHADUM;  
X:=ALPHANEW - 1;  
TMP:=X + FPF;  
TMP:=(X + HALF)*LN(TMP) - TMP;  
SER:=ONE;  
FOR I := 1 TO 6 DO  
    BEGIN  
        X:=X+ONE;  
        SER:=SER + COF[I]/X  
    END;  
GAMMALN:= (TMP + LN(STP*SER));  
GAM:=GAMMALN  
END;
```

```
FUNCTION FQ(LOAD,GAMMA1,XBT, GAMFCN,ALPHA,TCKNESS,WIDTH:REAL):REAL;
```

```
{COMPUTES THE TERMS OF THE INTEGRAND EXCEPTING THE SUMMATION}
```

```
CONST
```

```
S = 0.117;
```

```
K2 = 0.65;
```

```
YE = 9E9;
```

```
VAR
```

```
W,B,JIQ,FQ1,FXW,XC,SIG,INNER, INNER2:REAL;
```

```
BEGIN
```

```
B:=TCKNESS/1000;
```

```
W:=(WIDTH + 0.1)/1000;
```

```
SIG:=((LOAD*S)/(SQR(W)*B));
```

```
XC:=XBT/W;
```

```
FXW:= 1.122 - 1.4*(XC) + 7.33*SQR(XC) - 13.08*SQR(XC)*XC + 14*SQR(XC)*SQR(XC);
```

```
FXW:=SQR(FXW);
```

```
JIQ:=(SQR(SIG)*XBT*PI*FXW)/YE;
```

```
INNER:=((GAMFCN)*(JIQ/(2*GAMMA1) - K2)/(1 - K2));
```

```
IF INNER > 50 THEN
```

```
    FQ1:=0;
```

```
IF INNER < 0 THEN
```

```
    FQ1:=1
```

```
ELSE
```

```
    BEGIN
```

```
        INNER2:=ALPHA*LN(INNER);
```

```
        IF INNER2 > 3 THEN
```

```
            FQ1:=0
```

```
        ELSE
```

```
            FQ1:=EXP(-EXP(INNER2))
```

```
        END;
```

```
FQ:=FQ1
```

```
END;
```

```
FUNCTION SIMPSON(LOAD,GAMMA1,ALPHA,GAMFCN,TCKNESS,WIDTH,NLENGTH:REAL):REAL;
```

```
{EVALUATES THE INTEGRAL TERM USING SIMPSON'S RULE}
```

```
VAR
```

```
COUNT:INTEGER;
```

```
XB,XBT,SUM,B1,DX,SIMPSON1:REAL;
```

```
BEGIN
```

```
B1:= WIDTH/1000;
```

```
XB:= NLENGTH/1000;
```

```
SUM:=0;
```

```
DX:=(B1-XB)/100;
```

```
SUM:=FQ(LOAD,GAMMA1,XB,GAMFCN,ALPHA,TCKNESS,WIDTH)+FQ(LOAD,GAMMA1,B1,GAMFCN,ALPHA,TCKNESS,WIDTH);
```

```
XBT:=XB + DX;
```

```
WHILE XBT < B1 DO
```

```
    BEGIN
```

```
        SUM:= SUM + 4*FQ(LOAD,GAMMA1,XBT,GAMFCN,ALPHA,TCKNESS,WIDTH);
```

```
        XBT:=XBT + 2*DX
```

```
    END;
```

```
XBT:=XB + 2*DX;
```

```
WHILE XBT < B1 DO
```

```
    BEGIN
```

```
        SUM:= SUM + 2*FQ(LOAD,GAMMA1,XBT,GAMFCN,ALPHA,TCKNESS,WIDTH);
```

```
        XBT:= XBT + 2*DX
```

```
    END;
```

```
SIMPSON1:=DX*SUM/3;
```

```
SIMPSON:=SIMPSON1
```

```
END;
```

```
PROCEDURE ALLVALS(CMAX:REAL;GIMMERECDATAREC;VAR GFOUND, AFOUND:REAL);
```

```
VAR
```

```
FOUND : BOOLEAN;
```

```
INDEX : INTEGER;
```

```
BEGIN
```

```
INDEX:=1;
```

```
FOUND:=FALSE;
```

```
WHILE NOT FOUND DO
```

```
    IF CMAX = GIMMERECDATAREC[INDEX] THEN
```

```
        BEGIN
```

```
            FOUND:=TRUE;
```

```
            GFOUND:=GIMMERECDATAREC.DGAMMA[INDEX];
```

```
            AFOUND:=GIMMERECDATAREC.DALPHA[INDEX]
```

```
        END
```

```
    ELSE
```

```
        INDEX:=INDEX + 1
```

```
END;
```

```
FUNCTION MIN(FIRST,SECOND:REAL):REAL;
```

```
BEGIN
```

```
IF FIRST > SECOND THEN
```

```
    MIN:=SECOND
```

```
ELSE
```

```
    MIN:=FIRST
```

```
END;
```

```
PROCEDURE BUBSORT(GIMMERECDATAREC;VAR CMAX:REAL);
```

```
VAR
```

```
INDEX: INTEGER;
```

```
BEGIN
```

```
CMAX:=GIMMERECDATAREC[1];
```

```
INDEX:=1;
```

```
WHILE GIMMERECDATAREC[INDEX] <> 0 DO
```

```
    BEGIN
```

```
        CMAX:=MIN(GIMMERECDATAREC[INDEX],CMAX);
```

```
        INDEX:=INDEX + 1
```

```
    END;
```

```
END;
```

```
PROCEDURE GETDIMS(VAR TCKNESS, WIDTH, NLENGTH: REAL);
```

```
BEGIN
```

```
WRITE('WHAT IS THE SPECIMEN THICKNESS (MM)? ');
```

```
READLN(TCKNESS);
```

```
WRITE('WHAT IS THE SPECIMEN WIDTH (MM)? ');
```

```
READLN(WIDTH);
```

```
WRITE('WHAT IS THE NOTCH LENGTH (MM)? ');
```

```
READLN(NLENGTH)
```

```
END;
```

```
PROCEDURE FSTTERM(LOAD:QC;NPTS:INTEGER;GAMMA1,GAMMA2,ALPHA1,ALPHA2,ASTEP,GSTEP:REAL;
```

```
(COMPUTES THE F(Q) TERM IN KOLMOGOROV-SMIRNOV TEST)
```

```
CONST  
RUP=0.1E-3;
```

```
VAR  
FTERM,SIMPSON, CALVAL, GAMFCN:REAL;  
N, M, I : INTEGER;  
YUP, YDOWN : ARRAY[1..30] OF REAL;  
NEWVAL,ALPHADUM,YDIFF,TCKNESS,WIDTH,NLENGTH : REAL;
```

```
BEGIN
```

```
FOR N := 1 TO NPTS DO
```

```
  BEGIN  
    YUP[N]:= N/NPTS;  
    YDOWN[N]:=(N - 1)/NPTS  
  END;
```

```
  ALPHADUM:=ALPHA1;
```

```
  M:= 1;
```

```
  GETDIMS(TCKNESS,WIDTH,NLENGTH);
```

```
  WHILE GAMMA1 <= GAMMA2 DO
```

```
    BEGIN
```

```
      WHILE ALPHADUM <= ALPHA2 DO
```

```
        BEGIN
```

```
          NEWVAL:=0;
```

```
          FOR I:= 1 TO NPTS DO
```

```
            BEGIN
```

```
              CALVAL:=GAM(ALPHADUM);
```

```
              GAMFCN:=EXP(CALVAL);
```

```
              SIMPSON:=SIMPSON(LOAD[I],GAMMA1,ALPHADUM,GAMFCN,TCKNESS,
```

```
              FTERM:=EXP(-SIMPSON/RUP);
```

```
              WRITELN(FTERM:2:4);
```

```
              YDIFF:=ABS(FTERM - YUP[I]);
```

```
              IF YDIFF >= NEWVAL THEN
```

```
                NEWVAL:= YDIFF;
```

```
              YDIFF:=ABS(FTERM - YDOWN[I]);
```

```
              IF YDIFF >= NEWVAL THEN
```

```
                NEWVAL:= YDIFF
```

```
            END;
```

```
          WITH GIMMERECD DO
```

```
            BEGIN
```

```
              MAX[M]:=NEWVAL;
```

```
              DGAMMA[M]:=GAMMA1;
```

```
              DALPHA[M]:=ALPHADUM
```

```
            END;
```

```
          M:=M + 1;
```

```
          ALPHADUM := ALPHADUM + ASTEP
```

```
        END;
```

```
        GAMMA1:= GAMMA1 + GSTEP;
```

```
        ALPHADUM:= ALPHA1
```

```
      END;
```

```
    END;
```

```
PROCEDURE VAL(VAR GIMMERECDATAREC);
```

```
{COMPUTES AND RETAINS THE RESULT OF THE K-S TEST}
```

```
VAR
NPTS, I : INTEGER;
GAMMA1,GAMMA2,ALPHA1,ALPHA2,ASTEP,GSTEP:REAL;
LOAD : QC;

BEGIN
WRITE('NUMBER OF DATA POINTS? ');
READLN(NPTS);
WRITELN('INPUT THE CRITICAL LOADS FROM LOWEST TO HIGHEST: ');
FOR I := 1 TO NPTS DO
    READLN(LOAD[I]);
WRITE('STARTING VALUES FOR GAMMASTAR AND ALPHA? ');
READLN(GAMMA1,ALPHA1);
WRITE('ENDING VALUES FOR GAMMASTAR AND ALPHA? ');
READLN(GAMMA2,ALPHA2);
WRITE('STEP SIZE FOR GAMMASTAR AND ALPHA? ');
READLN(GSTEP,ASTEP);
FSTTERM(LOAD,NPTS,GAMMA1,GAMMA2,ALPHA1,ALPHA2,ASTEP,GSTEP,GIMMERECDATAREC)
END;
```

```
BEGIN
CLRSCR;
VAL(GIMMERECDATAREC);
BUBSORT(GIMMERECDATAREC,CMAX);
ALLVALS(CMAX,GIMMERECDATAREC,GFOUND,AFOUND);
WRITELN('DMAX = ',CMAX:1:3);
WRITELN('GAMMASTAR= ',GFOUND:4:1);
WRITELN('ALPHA= ',AFOUND:1:1)
END.
```